

On the growth and form of the gut

Thierry Savin^{1†*}, Natasza A. Kurpios^{2†*}, Amy E. Shyer^{2*}, Patricia Florescu¹, Haiyi Liang^{1†}, L. Mahadevan^{1,3,4,5,6,7} & Clifford J. Tabin²

The developing vertebrate gut tube forms a reproducible looped pattern as it grows into the body cavity. Here we use developmental experiments to eliminate alternative models and show that gut looping morphogenesis is driven by the homogeneous and isotropic forces that arise from the relative growth between the gut tube and the anchoring dorsal mesenteric sheet, tissues that grow at different rates. A simple physical mimic, using a differentially strained composite of a pliable rubber tube and a soft latex sheet is consistent with this mechanism and produces similar patterns. We devise a mathematical theory and a computational model for the number, size and shape of intestinal loops based solely on the measurable geometry, elasticity and relative growth of the tissues. The predictions of our theory are quantitatively consistent with observations of intestinal loops at different stages of development in the chick embryo. Our model also accounts for the qualitative and quantitative variation in the distinct gut looping patterns seen in a variety of species including quail, finch and mouse, illuminating how the simple macroscopic mechanics of differential growth drives the morphology of the developing gut.

Understanding morphogenesis, the origin of shape in anatomical structures, organs and organisms, has always been a central goal of developmental biology. Historically, the subject focused on the morphology and dynamics of embryonic growth¹, with many analogies to observable physical phenomena. This metaphoric approach to biological shape is epitomized in D'Arcy Thompson's *On Growth and Form*², with its focus on a mathematical and physical approach to the subject, emphasizing the role of differential growth in determining form. However, with the modern revolution in molecular biology, the field focused on a framework built around gene regulation, signalling molecules and transcription factors. This led to much insight into the logic of the developmental networks controlling processes as diverse as the patterning of the limb skeleton³ and the branching morphogenesis of the lung⁴. More recently, however, there has been a renewed appreciation of the fact that to understand morphogenesis in three dimensions, it is necessary to combine molecular insights (genes and morphogens) with knowledge of physical processes (transport, deformation and flow) generated by growing tissues.

In this context, there has been only recent limited exploration of the role of tissue-scale mechanical forces in organogenesis^{5–10}. Such large-scale forces can become important when the shape of an organ is remodelled after its initial structure has been formed. An important example of this hierarchy is the looping morphogenesis of the gut¹¹. The midgut forms as a simple linear tube of circular cross-section running down the midline of the embryo, and grows at a greater rate than the surrounding tissue, eventually becoming significantly longer than the trunk. As the size of the developing mid- and hindgut exceeds the capacity of the embryonic body cavity, a primary loop is forced ventrally into the umbilicus (in mammals) or yolk stalk (in birds). This loop first rotates anticlockwise by 90° and then by another 180° during the subsequent retraction into the body cavity. Eventually, the rostral half of the loop forms the midgut (small intestine) and the caudal half forms the upper half of the hindgut (the ascending colon).

The chirality of this gut rotation is directed by left–right asymmetries in cellular architecture that arise within the dorsal mesentery^{12–14}, an initially thick and short structure along the dorsal–ventral axis through which the gut tube is attached to the abdominal wall. This leads the mesentery to tilt the gut tube leftwards with a resulting anticlockwise corkscrewing of the gut as it herniates^{12,13}. However, the gut rotation is insufficient to pack the entire small intestine into the body cavity, and additional loops are formed as the intestine bends and twists even as it elongates. Once the gut attains its final form, which is highly stereotypical in a given species, the loops retract into the body cavity. During further growth of the juvenile, no additional loops are formed¹⁵, as they are tacked down by fascia, which restrict movement and additional morphogenesis without inhibiting globally uniform growth.

Relative growth between gut and attached mesentery drives looping

Throughout development, the gut tube remains attached to the body wall along its entire length by the dorsal mesentery, and is fixed at both its rostral and its caudal ends to the mouth and anus, respectively, resulting in the preservation of its connectivity and chirality during growth. The resulting number, shape and size of loops are also conserved in any given species, as shown in Fig. 1a for the chick at embryonic day 16 (E16).

In principle, this regularity of looping could result from either the intrinsic properties of the gut tube and mesentery or from external spatial packing constraints. However, surgical dissection of the gut and mesentery from the rest of the embryonic tissues shows that all the loops remain intact and identical to their *in ovo* structure at various stages of development (Fig. 1a), ruling out any role for body-cavity-induced constraints. Another possible mechanism for the reproducible looping is an increased asymmetric proliferation of cells in the gut tube at the locations of the bends. To test this, we counted the numbers of mitotic cells in the entire midgut section

¹School of Engineering and Applied Sciences, Harvard University, Cambridge, Massachusetts 02138, USA. ²Department of Genetics, Harvard Medical School, Boston, Massachusetts 02115, USA.

³Department of Organismic and Evolutionary Biology, Harvard University, Cambridge, Massachusetts 02138, USA. ⁴Department of Physics, Harvard University, Cambridge, Massachusetts 02138, USA.

⁵Department of Systems Biology, Harvard Medical School, Boston, Massachusetts 02115, USA. ⁶Wyss Institute for Biologically Inspired Engineering, Harvard University, Cambridge, Massachusetts 02138, USA. ⁷Kavli Institute for Bionano Science and Technology, Harvard University, Cambridge, Massachusetts 02138, USA. †Present addresses: Department of Materials, Polymer Physics, ETH Zürich, 8093 Zürich, Switzerland (T.S.); Department of Molecular Medicine, Cornell University, Ithaca, New York 14853, USA (N.A.K.); Department of Modern Mechanics, USTC-Hefei, Anhui 230027, China (H.L.).

*These authors contributed equally to this work.

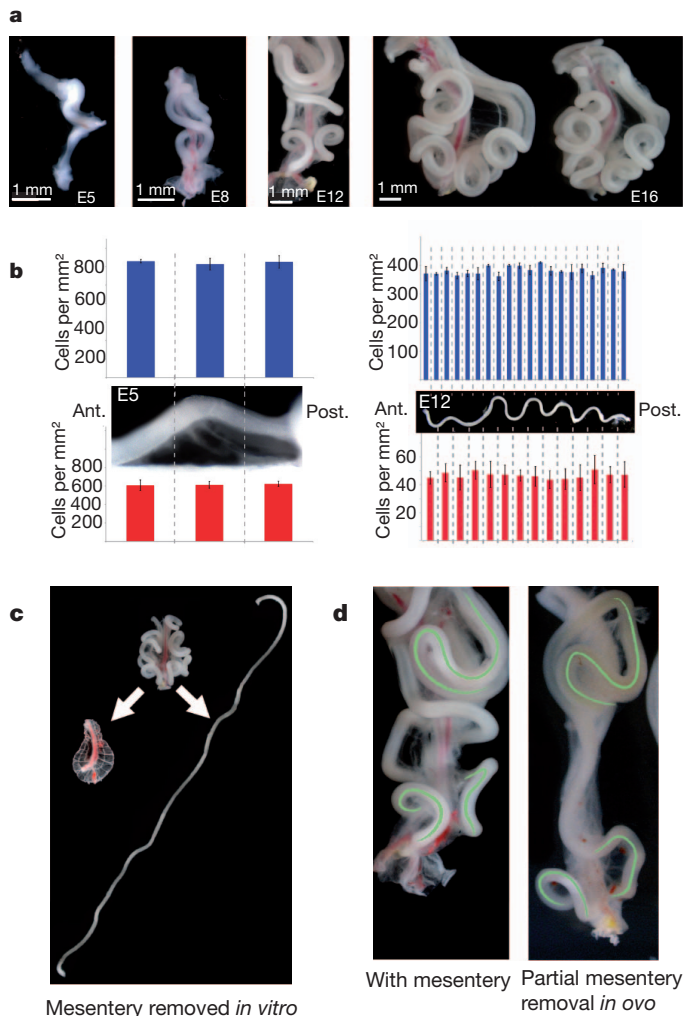


Figure 1 | Morphology of loops in the chick gut. **a**, Chick gut at embryonic day 5 (E5), E8, E12 and E16 shows stereotypical looping pattern. **b**, Proliferation in the E5 (left) and E12 (right) gut tubes (blue) and mesentery (red). Each blue bar represents the average number of phospho-H3-positive cells per unit surface in 40 (E5) or 50 (E12) 10- μ m sections. Each red bar represents the average number of phospho-H3-positive cells per unit surface over six 10- μ m sections (E5) or in specific regions demarcated by vasculature along the mesentery (E12). The inset images of the chick guts align the proliferation data with the locations of loops (all measurements were made in three or more chick samples). Ant., anterior; post., posterior. Error bars, s.d. **c**, The gut and mesentery before and after surgical separation at E14 show that the mesentery shrinks while the gut tube straightens out almost completely. **d**, The E12 chick gut under normal development with the mesentery (left) and after *in ovo* surgical separation of the mesentery at E4 (right). The gut and mesentery repair their attachment, leading to some regions of normal looping (green). However, a portion of the gut lacks normal loops as a result of disrupting the gut–mesentery interaction over the time these loops would otherwise have developed.

during the formation of the first loop at E5 (Fig. 1b) and later when there were nine loops (E12) (Fig. 1b). We observed consistently uniform proliferation with no significant differences along the rostrocaudal axis of the gut tube, including at loop formation locations and between loops, as well as no observable azimuthal or radial differences in proliferation rates at different cross-sections (Supplementary Fig. 1), consistent with observations that the embryonic gut tube cross-section remains circular along its length.

Because spatial constraints from the body cavity and the gut tube alone cannot explain the reproducible looping, we instead considered the dorsal mesentery, the webbed tissue that attaches the gut tube to

the embryo along its length. As looping morphogenesis is initiated, the dorsal mesentery changes from a thick, asymmetric, multilayer structure to a thin, double-epithelial sheet with no observable left–right asymmetry (Supplementary Fig. 2).

To test whether the dorsal mesentery is integral to the intestinal loops, we separated it from the gut surgically or enzymatically and found that the intestine uncoils into a straight tube, indicating that it was under compression. Simultaneously, the unconstrained dorsal mesentery contracts when freed from the gut tube (Fig. 1c), indicating that this tissue is under tension. Thus the gut–mesentery composite is required to maintain the mature loops in the gut.

To find out whether the dorsal mesentery is also required for the formation of the loops, we surgically separated a portion of the dorsal mesentery from the gut *in ovo*, beginning immediately caudal to the cranial (superior) mesenteric artery (SMA), at day E4, before loops develop. Strikingly, where the mesentery and gut were separated, the intestinal loops failed to form (Fig. 1d) even as normal loops formed in locations rostral and caudal to it (Fig. 1d, green lines). Although we were unable to cut the dorsal SMA *in ovo* during gut loop development, once the loops had matured (E12), surgical dissection of the SMA left the loops intact and in fact highlighted their periodic structure (Fig. 2c). This rules out any possible requirement for the SMA in directing loop structure, and for the vasculature as well, as secondary vessels develop only after the loops themselves have formed.

Although the gut grows uniformly, to investigate whether the mesentery might grow inhomogeneously and thus force the gut to loop at precise locations, we examined the proliferation rate of the mesentery at E5 and at E12. There were no observed differences along the rostrocaudal axis (Fig. 1b), suggesting that the growing mesentery exerts uniform compression along the length of the gut, countered by an equal and opposite tensile reaction on the mesentery from the gut.

Taken together, our observations suggest that uniform differential growth between the gut and the mesentery could be at the origin of loop formation. Because the gut tube is slender, with a length that is much larger than its radius, it responds physically to the differential strain-induced compression from the attached mesentery by bending and looping, while remaining attached to the embryo rostrocaudally. Most importantly, the fact that the gut relaxes to a straight configuration whereas the mesentery relaxes to an almost flat configuration implies that the tissues behave elastically, a fact that will allow us to quantify the process simply.

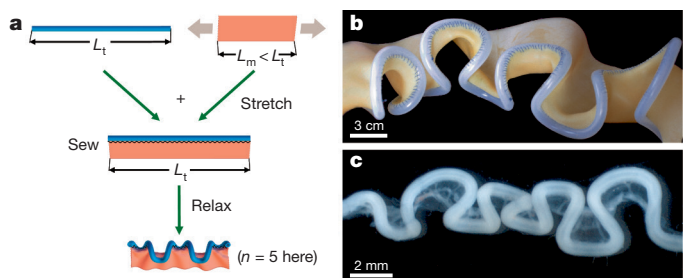


Figure 2 | Rubber simulacrum of gut looping morphogenesis. **a**, To construct the rubber model of looping, a thin rubber sheet (mesentery) was stretched uniformly along its length and then stitched to a straight, unstretched rubber tube (gut) along its boundary; the differential strain mimics the differential growth of the two tissues. The system was then allowed to relax, free of any external forces. **b**, On relaxation, the composite rubber model deformed into a structure very similar to the chick gut (here the thickness of the sheet is 1.3 mm and its Young's modulus is 1.3 MPa, and the radius of the tube is 4.8 mm, its thickness is 2.4 mm and its Young's modulus is 1.1 MPa; see Supplementary Information for details). **c**, Chick gut at E12. The superior mesenteric artery has been cut out (but not the mesentery), allowing the gut to be displayed aligned without altering its loop pattern.

Physical model of gut looping

To investigate the physical origins of this looping pattern, we developed a simple simulacrum of the gut–mesentery composite using a silicone rubber tube (mimicking the gut) and a thin latex sheet (mimicking the mesentery; see Supplementary Information). The differential strain induced by relative growth between the gut and the mesentery is simulated by extending the latex sheet along its length and stitching it to the wall of the naturally straight, unstretched rubber tube along the edge parallel to the direction of membrane stretching (Fig. 2a). On removing all external loads from the composite system, we observe the spontaneous formation of loops in the tube very similar in shape to the looping patterns seen *in ovo* (Fig. 2b). Varying the differential strain, the thickness of the latex sheet, the radius of the rubber tube and their material properties (Supplementary Information) shows that the wavelength and amplitude of the repeating loops depend only on these measurable parameters.

Scaling laws for loop period, radius and number

We now quantify the simple physical picture for looping sketched above to derive expressions for the size of a loop, characterized by the contour length, λ , and mean radius of curvature, R , of a single period (Fig. 3a). The geometry of the growing gut is characterized by the gut's inner and outer radii, r_i and r_o , which are much smaller than its increasing length, whereas that of the mesentery is described by its homogeneous thickness, h , which is much smaller than its other two dimensions. Because the gut tube and mesentery relax to nearly straight, flat states once they are surgically separated, we can model the gut as a one-dimensional elastic filament growing relative to a thin two-dimensional elastic sheet (the mesentery). As the gut length becomes longer than the perimeter of the mesentery to which it is attached, there is a differential strain, ε , that compresses the tube axially while extending the periphery of the sheet. When the growth strain is

larger than a critical value, ε_* , the straight tube buckles, taking on a wavy shape of characteristic amplitude A and period $\lambda \gg A$. At the onset of buckling, the extensional strain energy of the sheet per wavelength of the pattern is $U_m \propto E_m \varepsilon_*^2 h \lambda^2$, where E_m is the Young's modulus of the mesentery sheet. The bending energy of the tube per wavelength is $U_t \propto E_t I_t \kappa^2 \lambda$, where $\kappa \propto A/\lambda^2$ is the tube curvature, $I_t \propto r_o^4 - r_i^4$ is the moment of inertia of the tube and E_t is the Young's modulus of the tube. Using the condition that the in-plane strain in the sheet is $\varepsilon_* \propto A/\lambda$ and minimizing the sum of the two energies with respect to λ then yields a scaling law for the wavelength of the loop:

$$\lambda \propto \left(\frac{E_t I_t}{E_m h} \right)^{1/3} \quad (1)$$

The above theory is valid only at the onset of looping and cannot predict the amplitude or radius of a loop. Far from the onset of the instability, at a strain $\varepsilon = \varepsilon_0 \gg \varepsilon_*$, we use a torque balance argument to determine the finite radius of the loop. To deform the gut into a loop of radius R , the elastic torque required is $T_t \propto E_t I_t / R$ and must balance the torque exerted by the membrane with strain ε_0 over a width w and a length R , that is, $T_m \propto E_m h w \varepsilon_0 R$. The width of this strip is the radial distance from the tube over which the peripheral membrane stretching strain is relaxed, and is determined by the relation $\varepsilon_0 \propto w/(R - w)$. Balancing the torques, by equating T_t with T_m , and assuming that $\varepsilon_0 < 1$, yields the scaling law

$$R \propto \left(\frac{E_t I_t}{E_m h \varepsilon_0^2} \right)^{1/3} \quad (2)$$

Quantitative geometry and biomechanics of chick gut looping

A comparison of the results of our predictions with quantitative experiments requires the measurement of the geometry of the tissues,

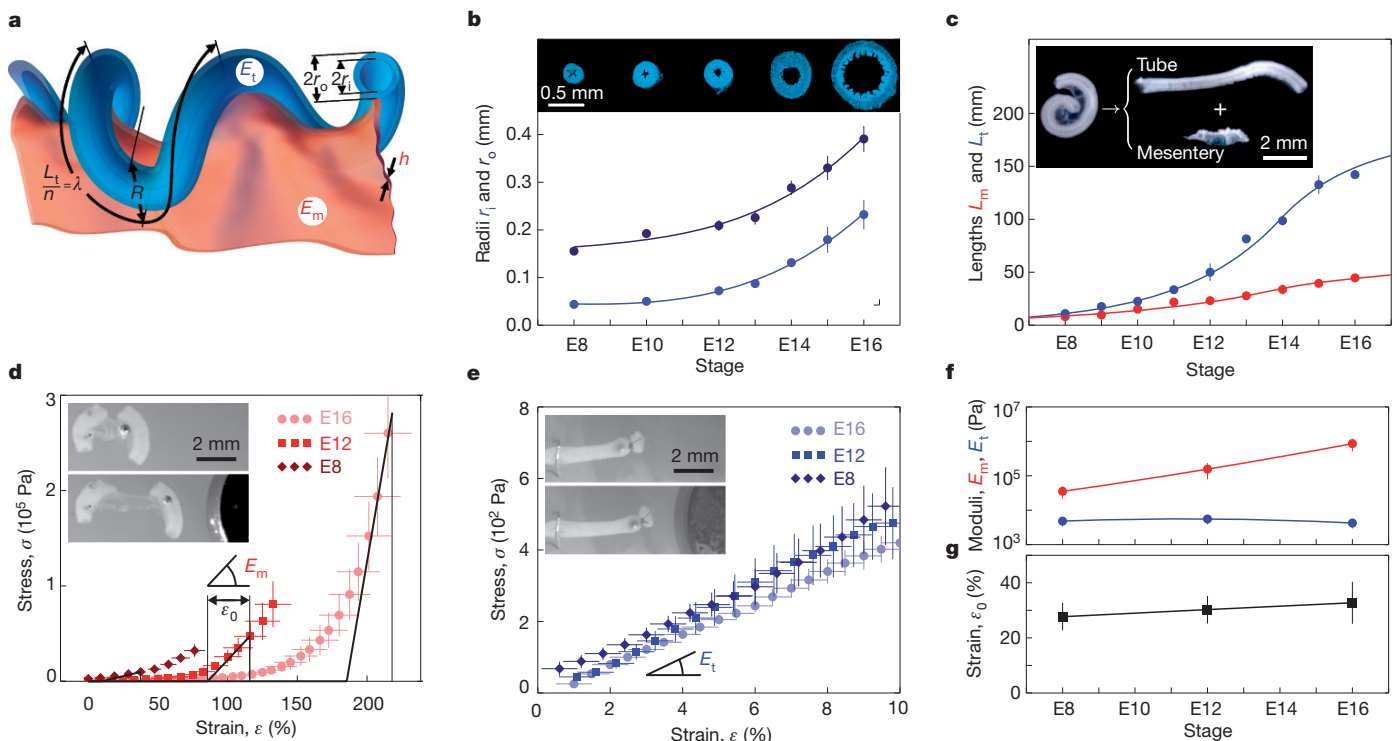


Figure 3 | Geometric and mechanical measurements of chick gut.

a, Parameters involved in the physical model. **b**, Inner (r_i , light blue) and outer (r_o , dark blue) tube diameters. Measurements are extracted from DAPI-stained tube cross-section shown in inset. **c**, Tube (length L_t , blue) and mesentery (length L_m , red) differential growth. Inset, length measurement of one isolated loop. **d**, Stress versus strain for the mesentery at E8, E12 and E16. For

physiological strains, we use the linearization shown by the black lines, to extract the effective Young's modulus, E_m , and the effective strain, ε_0 . **e**, Stress versus strain for the gut tube at E8, E12 and E16. **f**, Mesentery and tube Young's moduli, E_m (red) and E_t (blue), at E8, E12 and E16. **g**, Effective differential growth strain, ε_0 , at E8, E12 and E16. Error bars, s.d.

their elastic properties and the relative strain mismatch at different stages of chick gut development; we chose three stages: E8, E12 and E16 (Fig. 3). The mesentery has a time-varying thickness, h , which is evaluated from histological cross-section (Supplementary Fig. 2). The inner and outer radii of the gut tube were extracted from 4',6-diamidino-2-phenylindole (DAPI)-stained tube cross-sections (Fig. 3b). The length of the gut tube, L_t , was measured on the dissected gut. The natural rest length of the periphery of mesentery, L_m , was measured by cutting out thin strips along the junction with the gut and aligning them unstretched with a ruler (Fig. 3c). The bending stiffness of the gut tube and the stretching stiffness of the mesentery were measured using *in vitro*, uniaxial, low-rate tensile tests, where the load was generated by a magnet applying a calibrated force on a millimetre-size steel ball, attached to one end of a tissue sample that was pinned at the other end. The extension of the sample under load was tracked using video-microscopy to extract its stress (σ)/strain (ϵ) response curve (see Fig. 3d, e, insets, Methods and Supplementary Information).

For the mesentery, we observed a nonlinear response curve with a sharp break at a strain $\epsilon \leq \epsilon_p$, where $\epsilon_p = L_t/L_m - 1$ is the physiological strain mismatch, typical of the strain-stiffening seen in biological soft tissues¹⁶. We define an effective modulus, $E_m = (d\sigma/d\epsilon)_{\epsilon=\epsilon_p}$, and strain, $\epsilon_0 = (\sigma^{-1} d\sigma/d\epsilon)_{\epsilon=\epsilon_p}^{-1}$, by locally linearizing the response (Fig. 3d) and noting that the membrane has negligible stiffness when $0 < \epsilon < \epsilon_p - \epsilon_0$. For the gut, we measured the modulus, $E_t = \sigma/\epsilon$, from the linear, low-strain response curve ($\epsilon < 10\%$; Fig. 3e). In Fig. 3f, g, we summarize the variation of E_m , E_t and ϵ_0 as functions of developmental time. Measurements of the mesentery stiffness at various locations and in various directions did not show significant differences (Supplementary Fig. 4). This confirms the validity of modelling the mesentery and the gut as isotropic, homogeneous material.

The measured biophysical parameters allowed us to create a detailed numerical simulation of gut looping. Because the gut and mesentery grow slowly, inertial effects are unimportant and the composite system is always in mechanical equilibrium. This equilibrium configuration was calculated as follows. The mesentery was modelled as a discrete elastic membrane consisting of a hexagonal lattice of springs with a discrete energy associated with in-plane stretching/shearing deformations as well as out-of-plane bending deformations¹⁷, relative to the rest length of the springs. The gut was modelled as an equivalent membrane strip (two elements wide) with a discretized energy associated with bending and stretching deformations, and elastic stiffnesses different from those of the membrane. The geometry, mechanical properties and relative growth of the tissues parameterized by h , L_t , E_m , E_t and ϵ_0 were all experimentally measured at different time points during development. Given these input parameters, energy minimization for different relative growth strains, ϵ_0 , yielded predictions for the looping morphology of the gut (Methods and Supplementary Information).

In Fig. 4a, we compare the results of our observation at E16 with numerical simulations. In Fig. 4b, c, we compare our quantitative measurements of the wavelength and radius of curvature of the chick gut at the different measured stages of development (see also Supplementary Fig. 8) with those of both the rubber simulacrum and numerical simulations, as functions of the geometry and elastic moduli of the tube and sheet. Over the strain ranges $\epsilon_0 \in [0, 1]$ in the simulation (Supplementary Movie 1) and $\epsilon_0 \in [0.5, 1]$ for the various rubber models, we plot the wavelength, λ , and radius, R , of the loop and find that they follow the relations

$$\lambda \approx 36 \left(\frac{E_t L_t}{E_m h} \right)^{1/3} \quad (3)$$

$$R \approx 4 \left(\frac{E_t L_t}{E_m h \epsilon_0^2} \right)^{1/3} \quad (4)$$

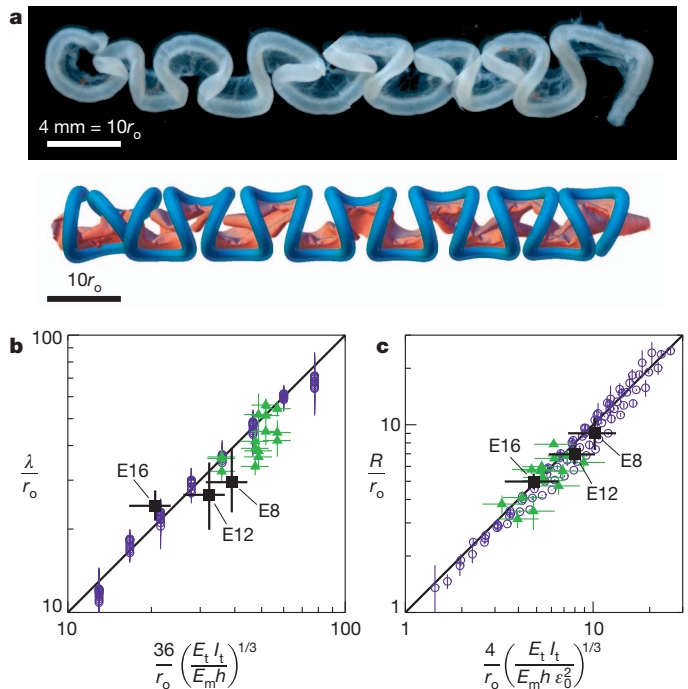


Figure 4 | Predictions for loop shape, size and number at three stages in chick gut development. **a**, Comparisons of the chick gut at E16 (top) with its simulated counterpart (bottom). **b**, Scaled loop contour length, λ/r_0 , plotted versus the equivalently scaled expression from equation (3) for the chick gut (black squares), the rubber model (green triangles) and numerical simulations (blue circles). The results are consistent with the scaling law in equation (1). **c**, Scaled loop radius, R/r_0 , plotted versus the equivalently scaled expression from equation (4) for the chick gut, the rubber model, and numerical simulations (symbols are as in **b**). The results are consistent with the scaling law in equation (2). Error bars, s.d.

in accord with our simple scaling laws (equations (1) and (2)). In Table 1, we compare the values of these parameters for the chick gut with the expressions given in equations (3) and (4), and confirm that our model captures the salient properties of the looping patterns with no adjustable parameters, strongly suggesting that the main features of the chick gut looping pattern are established by the simple balance of forces induced by the relative growth between the gut and the mesentery.

Comparative study of gut looping across species

To test our theory in cases other than the development of the chick gut, we took advantage of the distinct gut looping patterns observed in different avian taxa, which have served as criteria for phylogenetic classification and are thought of as having adaptive significance, independent of bird size.

Table 1 | Morphometry of chick gut looping pattern

Stage		n	λ (mm)	R (mm)
E8	Experimental observation	2.4 ± 0.4	4.6 ± 1.0	1.4 ± 0.2
	Computational model*	1.8 ± 0.3	6.1 ± 1.5	1.6 ± 0.3
E12	Experimental observation	9.0 ± 0.5	5.6 ± 1.2	1.5 ± 0.1
	Computational model†	7.3 ± 1.6	6.8 ± 1.6	1.7 ± 0.3
E16	Experimental observation	15.0 ± 0.5	9.5 ± 0.5	1.9 ± 0.1
	Computational model‡	17.5 ± 2.4	8.1 ± 1.9	1.9 ± 0.5

The observed number of loops (n), loop wavelength (λ) and radius (R) for the chick at different stages of gut development, for given geometrical and physical parameters associated with the gut and the mesentery, show that the model predictions are quantitatively consistent with observations.

* $L_t = 11.0 \pm 0.5$ mm, $h = 13.0 \pm 1.5$ μ m, $r_0 = 155 \pm 8$ μ m, $r_t = 44 \pm 5$ μ m, $E_m = 35 \pm 14$ kPa, $E_t = 4.8 \pm 1.4$ kPa, $\epsilon_p = 38 \pm 7\%$ and $\epsilon_0 = 28 \pm 5\%$.

† $L_t = 50.0 \pm 8.3$ mm, $h = 8.0 \pm 1.5$ μ m, $r_0 = 209 \pm 12$ μ m, $r_t = 72 \pm 9$ μ m, $E_m = 156 \pm 78$ kPa, $E_t = 5.6 \pm 1.7$ kPa, $\epsilon_p = 116 \pm 19\%$ and $\epsilon_0 = 30 \pm 5\%$.

‡ $L_t = 142.1 \pm 3.3$ mm, $h = 7.1 \pm 1.4$ μ m, $r_0 = 391 \pm 27$ μ m, $r_t = 232 \pm 31$ μ m, $E_m = 861 \pm 344$ kPa, $E_t = 4.2 \pm 1.3$ kPa, $\epsilon_p = 218 \pm 15\%$ and $\epsilon_0 = 33 \pm 8\%$.

We compared the gut looping patterns of the chick with those of the closely related (but differently sized) quail and those of a songbird, the zebra finch. In Fig. 5a, we see that, as previously described^{18,19}, the guts of the chick and the quail are organized almost identically but on different scales, and that the digestive tracts of songbirds and chickens are markedly different. To make the comparison quantitative, we repeated the morphometric and mechanical measurements (Supplementary Information) and used them to generate predictions from our scaling theory and computational model. In all cases, the predicted values of λ , R and n are again in excellent agreement with those observed in embryonic guts of the appropriate species (Fig. 5b, c and Table 2). For instance, we find that although growth strains, ε_p , are similar between the chick and the quail, the quail mesentery has a tension, $E_m h \varepsilon_0$, approximately five times greater than that in the chick mesentery. Qualitatively, this greater elastic force produces a smaller loop, hence inducing more loops per length and, thus, the same number of loops in the smaller bird. By contrast, most of the geometrical and physical parameters characterizing the developing gut and mesentery in the chick and the zebra finch are different and lead to different looping parameters.

Finally, to test our theoretical model with a non-avian example, we performed a similar set of measurements throughout the course of gut development in mouse embryos. In agreement with our findings from birds, the geometrical and biophysical properties of the developing gut and dorsal mesentery suffice to predict accurately the stereotypical patterns of the mature intestinal loops in mouse embryos (Fig. 5 and

Table 2 | Morphometry of quail, finch and mouse gut looping patterns

Species and stage		n	λ (mm)	R (mm)
Quail E12	Experimental observation	9.0 ± 0.7	4.6 ± 0.4	1.2 ± 0.1
	Computational model*	10.0 ± 1.3	4.1 ± 1.0	1.2 ± 0.3
Finch E13	Experimental observation	5.5 ± 0.5	3.6 ± 0.5	0.6 ± 0.3
	Computational model†	5.3 ± 0.8	3.7 ± 0.9	0.9 ± 0.2
Mouse E16.5	Experimental observation	6.0 ± 0.5	6.0 ± 0.7	0.7 ± 0.1
	Computational model‡	5.6 ± 0.8	6.4 ± 1.5	1.0 ± 0.1

The observed number of loops, loop wavelength and radius for the quail, finch and mouse, for given geometrical and physical parameters associated with the gut and the mesentery, show that the model predictions are quantitatively consistent with observations.

* $L_t = 41.3 \pm 0.4$ mm, $h = 14.9 \pm 1.6$ μ m, $r_0 = 248 \pm 13$ μ m, $r_t = 154 \pm 12$ μ m, $E_m = 515 \pm 206$ kPa,

$E_t = 4.4 \pm 1.3$ kPa, $\varepsilon_p = 110 \pm 13\%$ and $\varepsilon_0 = 23 \pm 5\%$.

† $L_t = 19.7 \pm 0.8$ mm, $h = 6.0 \pm 0.6$ μ m, $r_0 = 227 \pm 14$ μ m, $r_t = 120 \pm 13$ μ m, $E_m = 802 \pm 321$ kPa,

$E_t = 2.6 \pm 0.8$ kPa, $\varepsilon_p = 110 \pm 11\%$ and $\varepsilon_0 = 32 \pm 5\%$.

‡ $L_t = 35.9 \pm 0.9$ mm, $h = 12.3 \pm 1.6$ μ m, $r_0 = 270 \pm 16$ μ m, $r_t = 178 \pm 14$ μ m, $E_m = 94 \pm 37$ kPa,

$E_t = 1.9 \pm 0.9$ kPa, $\varepsilon_p = 200 \pm 13\%$ and $\varepsilon_0 = 64 \pm 5\%$.

Table 2). The mouse gut is notably characterized by softer tissues and higher mismatch strain, producing tightly coiled loops, as seen in Fig. 5a. The physiological stresses in the mesentery fall in the same range (Supplementary Information) in all the species investigated in this study, suggesting that both growth and the properties of tissues might be regulated by mechanical feedback.

Discussion

The developing intestine is a simple, elongated, tubular structure that is stereotypically and reproducibly folded into a compact organ through the process of looping morphogenesis. Using a combination of quantitative experiments, computations and scaling arguments, we have shown that the associated looping patterns are quantitatively determined by the differential growth between the gut tube and the dorsal mesentery and by their geometric and elastic properties, both within individual organisms and across species. We thus bring a quantitative biomechanical perspective to the mostly metaphoric arguments in *On Growth and Form*².

The simplicity of the mechanical origin in the diversity in gut looping patterns, long associated with the adaptive significance of the distinct diets and gut residence times of different animals¹⁸, also suggests that because it is sufficient to modulate the uniform tissue growth rates, tissue geometry and elasticity of the gut–mesentery system to change these patterns, this is the minimal set of properties on which selection has acted to achieve the looping patterns found in nature.

Identification of the relevant cellular parameters influencing gut morphogenesis opens the door to future studies of the genes involved in controlling cell proliferation and matrix formation in space and time, and sets the stage to understanding the processes by which biochemical and biophysical events across scales conspire to drive the developmental regulation of growing tissues.

METHODS SUMMARY

Embryos. Fertile chick eggs (White Leghorn eggs) were obtained from commercial sources. Fertile zebra finch eggs were provided by the laboratory of T. Gardner at Boston University. Fertile Japanese quail eggs were obtained from Strickland Game Bird. All eggs were incubated at 37.5 °C and staged following ref. 20. Mouse embryos were collected from staged pregnant females (Charles River Laboratories).

Immunohistochemistry and histology. Small intestines were collected from chick embryos at desired stages and fixed in 4% paraformaldehyde in PBS and embedded in paraffin wax. Immunohistochemistry and histology was performed on 10- μ m transverse sections of the gut tube.

In ovo gut surgeries. The gut tube and the dorsal mesentery were separated *in ovo* at stage 23–25 by using a pulled glass needle to cut the connection between the two tissues. Embryos were re-incubated until E12, when they were collected to examine the resulting looping pattern.

Mechanical properties of gut and mesentery tissue. The force, $F(d)$, between a permanent magnet (The Magnet Source) and millimetre-size steel balls (New England Miniature Ball Corp.), separated by a distance d , was calculated from the damped motion of the ball rising in glycerol with the magnet lowered from

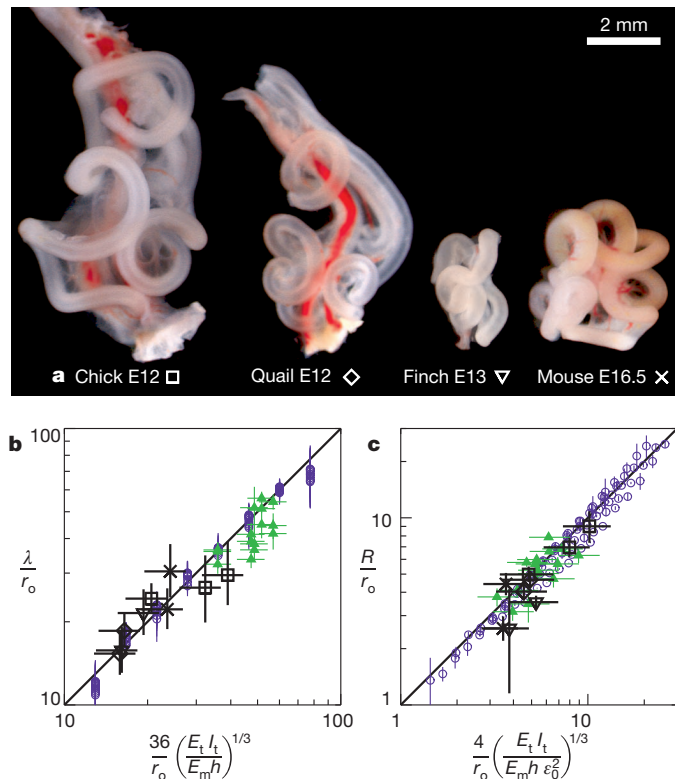


Figure 5 | Comparative predictions for looping parameters across species. **a**, Gut looping patterns in the chick, quail, finch and mouse (to scale) show qualitative similarities in the shape of the loops, although the size and number of loops vary substantially. **b**, Comparison of the scaled loop contour length, λ/r_0 , with the equivalently scaled expression from equation (3) shows that our results are consistent with the scaling law in equation (1) across species. Black symbols are for the animals shown in **a**, other symbols are the same as in Fig. 4b. **c**, Comparison of the scaled loop radius, R/r_0 , with the equivalently scaled expression from equation (4) shows that our results are consistent with the scaling law in equation (2) across species (symbols are as in **b**). In **b** and **c**, points are reported for chick at E8, E12 and E16; quail at E12 and E15; finch at E10 and E13; and mouse at E14.5 and E16.5. Error bars, s.d.

above. For $2\text{ mm} < d < 8\text{ mm}$, the range used in the subsequent measurements, $F(d)$ ranges from $1\text{ }\mu\text{N}$ to 1 mN . We then surgically extracted strips of the mesentery and sections of the gut tube from fresh animal embryos. A steel bead was attached at one end of the sample, by either gluing it onto the strip or sealing it into the tube. With the other end of the sample pinned to an agarose gel, the magnet was moved closer to stretch the sample while d and the extension, L , of the sample were tracked by video. We then calculated the stress, $\sigma = F(d)/A_0$, and the strain, $\varepsilon = L/L_0 - 1$, where L_0 and A_0 are respectively the length and the cross-sectional area of the sample at rest. All dissections, manipulations and tensile tests occurred in Ringer buffer (Sigma Aldrich), and within hours after the surgery.

Full Methods and any associated references are available in the online version of the paper at www.nature.com/nature.

Received 23 January; accepted 7 June 2011.

1. His, W. *Anatomie Menschlicher Embryonen* (Vogel, 1880).
2. Thompson, D. W. *On Growth and Form* (Cambridge Univ. Press, 1917).
3. Johnson, R. L. & Tabin, C. J. Molecular models for vertebrate limb development. *Cell* **90**, 979–990 (1997).
4. Metzger, R. J. & Krasnow, M. A. Genetic control of branching morphogenesis. *Science* **284**, 1635–1639 (1999).
5. Hufnagel, L. *et al.* On the mechanism of wing size determination in fly development. *Proc. Natl Acad. Sci. USA* **104**, 3835–3840 (2007).
6. Beloussov, L. V. *et al.* Mechanical stresses in embryonic tissues: patterns, morphogenetic role, and involvement in regulatory feedback. *Int. Rev. Cytol.* **150**, 1–34 (1994).
7. Taber, L. A. Biomechanics of cardiovascular development. *Annu. Rev. Biomed. Eng.* **3**, 1–25 (2001).
8. Salazar-Ciudad, I. & Jernvall, J. A computational model of teeth and the developmental origins of morphological variation. *Nature* **464**, 583–586 (2010).
9. Hamant, O. *et al.* Developmental patterning by mechanical signals in *Arabidopsis*. *Science* **322**, 1650–1655 (2008).
10. Forgacs, G. & Newman, S. *Biological Physics of the Developing Embryo* (Cambridge Univ. Press, 2005).
11. Schoenwolf, G. *et al.* *Larsen's Human Embryology* Ch. 14 (Elsevier Health Sciences, 2008).
12. Kurpios, N. A. *et al.* The direction of gut looping is established by changes in the extracellular matrix and in cell:cell adhesion. *Proc. Natl Acad. Sci. USA* **105**, 8499–8506 (2008).
13. Davis, N. M. *et al.* The chirality of gut rotation derives from left-right asymmetric changes in the architecture of the dorsal mesentery. *Dev. Cell* **15**, 134–145 (2008).
14. Hecksher-Sorensen, J. *et al.* The splanchnic mesodermal plate directs spleen and pancreatic laterality, and is regulated by *Bapx1/Nkx3.2*. *Development* **131**, 4665–4675 (2004).
15. Kleinman, R. E. *et al.* *Walker's Pediatric Gastrointestinal Disease* 207–216 (Decker, 2008).
16. Fung, Y. C. *Biomechanics: Mechanical Properties of Living Tissues* 2nd edn, 242–320 (Springer, 2004).
17. Liang, H. & Mahadevan, L. The shape of a long leaf. *Proc. Natl Acad. Sci. USA* **106**, 22049–22054 (2009).
18. Beddard, F. E. *The Structure and Classification of Birds* (Longmans, Green and Co., 1898).
19. Mitchell, C. P. On the intestinal tract of birds. *Proc. Zool. Soc. Lond.* **64**, 136–159 (1896).
20. Hamburger, H. & Hamilton, H. L. A series of normal stages in the development of the chick embryo. *J. Exp. Morphol.* **88**, 49–92 (1951).

Supplementary Information is linked to the online version of the paper at www.nature.com/nature.

Acknowledgements We thank R. Prum for pointing out to us the literature on avian intestines, and the Harvard NSF MRSEC, the MacArthur Foundation (L.M.) and NIH RO1 HD047360 (C.J.T.) for support.

Author Contributions C.J.T., N.A.K. and L.M. designed the research with additional contributions from T.S. and A.E.S.; T.S. (biophysical and computational experiments, data analysis), N.A.K. (biological experiments), A.E.S. (biological and biophysical experiments) and L.M. (physical mechanism, physical/mathematical model, scaling theory) did the research; P.F. (stitched physical model) and H.L. (built computational model) contributed tools; and T.S., N.A.K., L.M. and C.J.T. wrote the paper.

Author Information Reprints and permissions information is available at www.nature.com/reprints. The authors declare no competing financial interests. Readers are welcome to comment on the online version of this article at www.nature.com/nature. Correspondence and requests for materials should be addressed to L.M. (lm@seas.harvard.edu).

METHODS

Embryos. Fertile chick eggs (White Leghorn eggs) were obtained from commercial sources. Fertile zebra finch eggs were provided by the laboratory of T. Gardner at Boston University. Fertile Japanese quail eggs were obtained from Strickland Game Bird. All eggs were incubated at 37.5 °C and staged following ref. 20. Mouse embryos were collected from staged pregnant females (Charles River Laboratories).

Immunohistochemistry and histology. Small intestines were collected from chick embryos at desired stages and fixed in 4% paraformaldehyde in PBS and embedded in paraffin wax, allowing for 10-µm transverse sections of the gut tube. Fast green staining was performed as described in ref. 20. Immunohistochemistry was performed with rabbit polyclonal antiphospho-H3 (1:100) (Millipore) overnight at 4 °C in PBS containing 3% goat serum and 0.1% Triton X-100. Sections were next incubated with Alexa Fluor 594 goat anti-rabbit secondary antibody (1:300; Molecular Probes) for 1 h at room temperature (25 °C). DAPI (Molecular Probes) was used as a nuclear counterstain and to determine the inner and outer radii of the gut tube.

In ovo gut surgeries. The gut tube and the dorsal mesentery were separated *in ovo* at stage 23–25 (ref. 20) by using a pulled glass needle to cut the connection between the two tissues. Most, but not all, of the connection was ablated as care was taken to avoid puncturing the dorsal aorta, which runs over the gut tube and dorsal mesentery at this stage. Embryos were re-incubated until E12, when they were collected to examine the resulting looping pattern.

Physical simulacrum using rubber. We used wide strips of elastic rubber sheeting (McMaster-Carr) of various thicknesses. Each strip was held stretched in one direction at the desired extension using clamps, and a silicon rubber tube (NewAge Industries) was stitched to the sheet using sewing thread (Supplementary Information).

Calibration of the magnetic force. The attractive interaction between a permanent disc magnet (commercial grade, axially magnetized, neodymium Nd-Fe-B; The Magnet Source) and high-precision steel balls (AISI 440C stainless steel, radii $r_b = 0.122, 0.253$ and 0.398 mm; New England Miniature Ball Corp.) was calibrated using a ‘falling-ball viscometer’ geometry: immersed in a tube filled with pure glycerol, the magnet is brought closer to the ball from above, and the ball consequently rises (we ensured that all materials used to manipulate the beads and the magnet during the measurements, calibration and tensile tests had no magnetic susceptibility). The force exerted by the magnet is balanced by gravity, drag and inertia. At low Reynolds number, drag force and inertia can be measured from the ball trajectory that is extracted using video tracking (see details in the Supplementary Information). We can then calculate the attractive force, $F(d)$, between the magnet and the ball as a function of their separation distance, d . We report our results in Supplementary Fig. 3 and Supplementary Table 1. Notably, for the distances, $2 \text{ mm} < d < 8 \text{ mm}$, used in the tissue tensile test, the force ranges from $1 \mu\text{N}$ to 1 mN .

Measurements of tissue mechanical properties. We surgically dissected fragments of the mesentery and of the gut tube from live embryos. Samples of the mesentery were cut out to leave a well-defined, millimetre-width strip with principal axis either perpendicular to the tube (radial measurement) or parallel to the tube (tangential measurement). For mesentery fragments, the steel beads were glued using synthetic glue (Instant Krazy Glue) at one end of the tissue strip. The other end was pinned to an agarose gel layer. During the dissection of the sample, we kept sections of the tube or of the superior mesenteric artery to provide convenient handles to which to attach the bead (see Fig. 3d and Supplementary

Fig. 4, where sections of the tube are visible). For gut tube fragments, the steel beads were inserted into the tube and secured by tying the lumen using a hair with an overhand knot. The other end of the tube was held on the agarose gel using a horseshoe pin (Fig. 3e and Supplementary Fig. 5). All dissections, manipulations and tensile tests were performed in Ringer buffer (Sigma Aldrich), and the measurements were made within a few hours of the dissection.

The magnet was attached to a plastic arm held on a micrometric translation stage, and moved closer to the sample on the agarose gel (Supplementary Fig. 4a). The magnet attracted the steel bead and stretched the sample in a controlled fashion (Supplementary Movie 2). The tensile tests were video-recorded to track the extension, L , of the sample and the bead–magnet distance, d , and were run as follows. The sample was first pre-conditioned by stretching it once to an extension ratio greater than one, after which the magnet was removed to let the sample relax to its rest length, L_0 (Supplementary Movie 2), at which stage we measured the rest width, w_0 , of the mesentery sample. The magnet was then moved back towards the sample in a stepwise manner. At each step, the sample stretched and was confirmed visually to have reached equilibrium extension before the next step was taken. We thus effectively measured the static elasticity of the tissue, in terms of the nominal stress, $F(d)/A_0$, produced by a nominal strain, $\varepsilon = L/L_0 - 1$. Here A_0 is the cross-section of the sample at rest: $A_0 = w_0(1 + \varepsilon_p)^{1/2}h$ for the mesentery, by virtue of material incompressibility, and $A_0 = \pi(r_o^2 - r_i^2)$ for the tube.

We verified that this method gives reproducible results, and we found that the same-sample variations were less than sample-to-sample variations that we measured at about 50%. Several stress–strain response curves, corresponding to samples of mesentery and gut tubes extracted from different chick E16 embryos are shown in Supplementary Figs 4c and 5b and indicate the level of reproducibility.

Computational model. The mesentery was modelled as a hexagonal lattice of linear springs with rest length a_m , whose discrete energy

$$F_m = \frac{\sqrt{3}E_m h}{4} \sum_{ij} (r_{ij} - a_m)^2 + \frac{E_m h^3}{12\sqrt{3}} \sum_{\alpha\beta} (\mathbf{n}_\alpha - \mathbf{n}_\beta)^2$$

accounts for in-plane stretching (first term, where r_{ij} is the spring length between nodes i and j) and out-of-plane bending (second term, where \mathbf{n}_α is the unit normal vector to the triangular facet), and tends to the energy of an elastic membrane of thickness h and Young’s modulus E_m as $a_m \rightarrow 0$ (ref. 17). The gut tube was modelled with a similar, but two-element-wide, lattice of springs with rest length a_t . The discrete energy

$$F_t = \frac{5.6\sqrt{3}E_t I_t}{8r_o^3} \sum_{ij} (r_{ij} - a_t)^2 + \frac{E_t I_t}{2r_o\sqrt{3}} \sum_{\alpha\beta} (\mathbf{n}_\alpha - \mathbf{n}_\beta)^2$$

of this strip also contains in- and out-of-plane deformations terms (first and second terms, respectively), which are chosen such that the in- and out-of-plane bending stiffnesses both converge to $E_t I_t$ for a tube of outer radius r_o (see details in Supplementary Information). At various time points in the development of the gut (E8, E12 and E16), the parameters h , I_t , E_m , E_t and ε_0 are all experimentally measured and input into the energy, with the relative growth, $\varepsilon_0 = a_m/a_t - 1$, imposing the mismatch strain between the membrane and the tube attached to it. Then the energy $F_m + F_t$ is minimized using a damped molecular dynamics algorithm¹⁷, to yield the equilibrium configuration of the gut–mesentery composite system.

Supplementary Information for “On the growth and form of the gut” by T. Savin et al.

Cell proliferation along the gut

To characterize cell proliferation in the gut, we used a mitotic marker (see the “Methods” section of the main text) and find that there is no asymmetric proliferation in cross sections of the gut at different positions along it as shown in Figure S1.

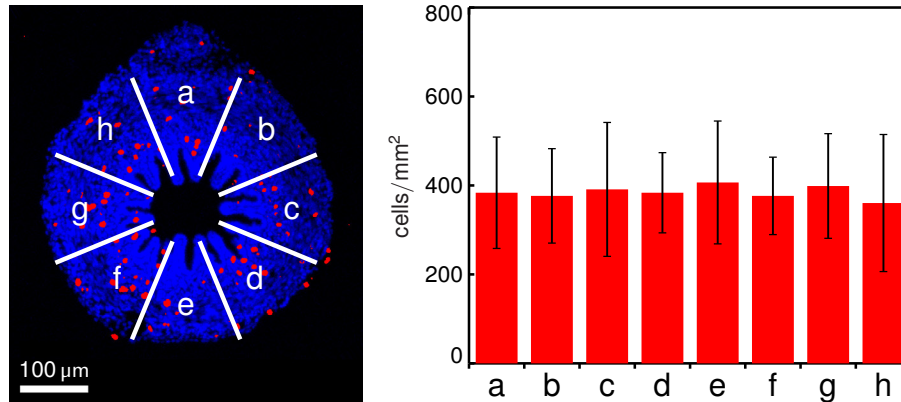


Figure S1 | Cell proliferation patterns in a cross-section of the tube at E12. Ten tube sections, stained for cell nuclei (blue) and mitosis (red), and extracted from approximately equidistant locations along the extent of the entire tube, were each divided into 8 equal slices labelled, as shown, such that the connection with the mesentery is at slice “a” (the “12 o’clock” position). The number of cells per unit area was extracted in each slice and averaged across the sections. We cannot detect different proliferation between the slices, thus validating the radial symmetry of tube growth. Error bars, s.d.

Mesentery histology and thickness

Embryos were fixed in 4% paraformaldehyde and then dehydrated in a graded ethanol series, cleared in xylenes, and embedded in paraffin. Sections at 10 μm thickness were collected. Fast Green staining was performed using standard protocols: briefly, slides were dewaxed in xylenes, rinsed in successive washes with 100% and 95% ethanol, and rehydrated in tap water. Slides were then stained with Fast Green (Sigma Aldrich) for 30 minutes, rinsed in tap water, dehydrated, cleared in xylenes and sealed with DPX mountant (Fluka). Micrographs of these sections are shown in Figure S2 and were used to measure the mesentery thickness h reported in Figs. S9a to S11a.

Physical simulacrum of gut looping using rubber tubes and sheets

To mimic the differential strain induced by differential growth between the gut tube and the mesentery, we used a rubber membrane-strip that was stretched longitudinally and stitched to a naturally straight, unstretched rubber tube, and then allowed the composite to relax to equilibrium while preventing the ends from twisting or otherwise rotating. This preserves the topology of the composite system, puts the gut under compression and the membrane under tension, and leads to looping patterns identical to those seen in the real gut.

We cut wide strips of elastic rubber sheet (McMaster-Carr) of various thicknesses (width > 10 cm, length about 1 m, and thicknesses of 0.25, 0.4, 1 and 1.3 mm). An individual sheet was held stretched in one direction at the desired extension using clamps. For extension ratios up to 2, we verified that the mechanical response of the rubber is linear. Silicon rubber tubes of radii $r_i = r_o/2$, with $r_o = 4.77$ and 1.59 mm (NewAge Industries,

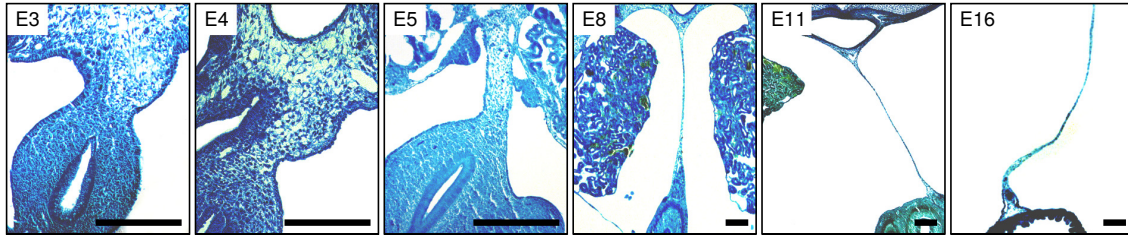


Figure S2 | Cellular morphology of the mesentery during gut development. The dorsal mesentery undergoes cellular rearrangement in the course of gut development during which the asymmetric cellular morphology first seen at E3 of embryonic development is lost and the mesentery consists of only few layers of mesothelium as seen in cross-section of the mature gut (E16). All scale bars represent 100 μm .

inc.), were stitched to the sheet using sewing thread. Upon relaxing the sheet, we observed the spontaneous formation of loops. We verified that the loop radius was always much smaller than the width of the sheet, and also much smaller than the natural radius of the tubes that is associated with residual strains from packaging/transportation, thus qualitatively similar to the real gut-mesentery system. The Young's modulus of the sheet ($E_m = 1.3 \pm 0.2 \text{ MPa}$) and of the tube ($E_t = 1.1 \pm 0.3 \text{ MPa}$) were measured using simple extensional tests.

Admittedly the mesentery and the gut tube are microstructurally far more complex living materials than the simple latex and rubber used in the physical model. Yet, at the mesoscopic length scale of a loop that is much larger than that of local cellular or multicellular heterogeneities (e.g. vessels, collagen fibers) but smaller than the whole gut, these effects average out and allow us to isolate the essential mechanics of the formation of loops in terms of elastic forces driven by the strain mismatch arising from differential growth.

Calibration of magnetic bead force-extension curve

We used the attractive force between a permanent magnet and a millimeter size steel bead attached to the tissue to measure the mechanical properties of the gut and mesentery at different stages of development. This allowed us to apply forces in the $10^{-6} - 10^{-3} \text{ N}$ range on millimetric biological samples and characterize the stress-strain relation of the tissues.

To calibrate the magnetic force vs. distance curve, we used the known resistance to motion of a steel ball (AISI 440C martensitic stainless steel, density $\rho_b = 7650 \text{ kg} \cdot \text{m}^{-3}$, radius $r_b = 0.122, 0.253$ or 0.398 mm , $\pm 0.01 \text{ mm}$; New England Miniature Ball Corp.) in pure glycerol (density $\rho_f = 1260 \text{ kg} \cdot \text{m}^{-3}$, viscosity $\eta_f = 0.690 \text{ Pa} \cdot \text{s}$ at 29°C). When the ball was placed at the tip of a conical support and a disc magnet (commercial grade, neodymium Nd-Fe-B, diameter $2r_m = 7.5 \text{ mm}$, height 2.8 mm , nickel plated; The Magnet Source) was then brought above the bead (cylindrical edges facing the bead, vertical flat edges) we observed the motion of the ball which was recorded at 250 frames per second using a digital camera (PL-B781, PixeLINK) equipped with an objective that effectively magnified to 0.045 mm per pixel. All materials used to manipulate the beads and the magnet during the measurements had no magnetic susceptibility. Movies were then processed off-line using the IDL language (ITT Visual Information Solutions) to extract the position of the bead and of the magnet. We used a particle tracking package [1] to extract the bead trajectory. Tracking the magnet was performed by using image registration of a reference sub-array in each frames. The reference image was manually clipped from the initial frame to contain the intensity pattern of the feature (here, the magnet) to be tracked. It was then aligned in the remaining frames onto the “mobile” matching pattern by maximizing intensity correlation [2]. These trajectory extraction methods offer a resolution that we estimated to be about $1/2 \text{ pixel}$, i.e. $\sim 20 \mu\text{m}$.

To quantify the forces associated with this motion, we used the known analytic description of the dynamics of the steel ball in a viscous fluid [3],

$$\frac{4}{3}\pi r_b^3 \left(\rho_b + \frac{\rho_f}{2} \right) \dot{v}(t) = F - 6\pi\eta_f r_b v(t) - \frac{4}{3}\pi r_b^3 (\rho_b - \rho_f)g - 6r_b^2 (\pi\eta_f \rho_f)^{1/2} \int_0^t \frac{\dot{v}(\tau) d\tau}{(t-\tau)^{1/2}},$$

where the rate of change of the momentum of the bead (left-hand side) is balanced by, in order of appearance in

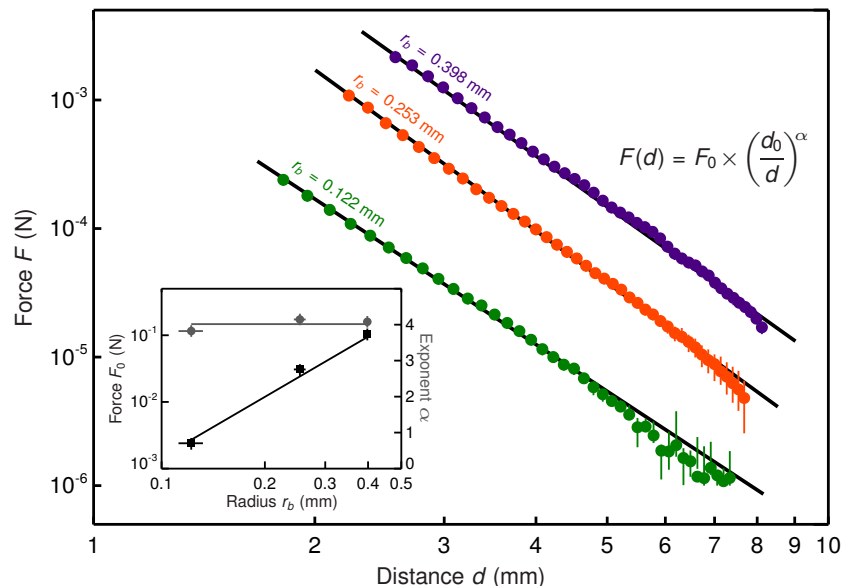


Figure S3 | Calibration of the magnet-bead force-displacement curve. The force vs. distance calibration curves for 3 different sizes of the steel magnetizable bead. The parameters for the power-law fit $F(d) = F_0(d/d_0)^\alpha$ are shown in inset; the force is shown on the left ordinate while the exponent is shown on the right. Error bars, s.d.

the right-hand side: the magnetic force F (to be determined), the drag force, the weight, and the Boussinesq-Basset force. Here $v(t)$ and $\dot{v}(t)$ are respectively the velocity and acceleration of the bead at time t and $g = 9.81 \text{ m} \cdot \text{s}^{-2}$ is the gravity¹. We verified that the Reynolds number $\frac{\rho_f r_b v}{\eta_f} < 10^{-1}$ at all times, so that the fluid inertial contributions are small and can be neglected in the above equation. Then the magnetic force is balanced by the Stokes drag and gravity and can thus be measured from the bead trajectory as a function of the bead-magnet distance d , between the ball's center and the cylindrical edge of the magnet, and is shown in Figure S3. We find that over the range of distance $2 < d < 8 \text{ mm}$, the force follows a power-law scaling $F(d) = F_0(d_0/d)^\alpha$, where we parametrize the power-law fit using the characteristic magnitude of the force $F_0 = F(d = d_0)$ at the characteristic distance $d_0 = 1 \text{ mm}$. The results are summarized in table S1.

r_b	F_0	α
$0.122 \pm 0.010 \text{ mm}$	$(2.40 \pm 0.2) \times 10^{-3} \text{ N}$	3.76 ± 0.2
$0.253 \pm 0.010 \text{ mm}$	$(3.07 \pm 0.3) \times 10^{-2} \text{ N}$	4.16 ± 0.2
$0.398 \pm 0.010 \text{ mm}$	$(1.05 \pm 0.1) \times 10^{-1} \text{ N}$	4.08 ± 0.2

Table S1 | Power-Law fitting parameters for the bead-magnet interaction force. We observe that the scaling follows closely $F \propto r_b^3 d^{-4}$ (see inset of Fig S3).

We verified that the curves were reproducible for different beads of the same batch, and were unchanged whether or not the steel balls were in contact with the magnet prior to the measurement. Finally, we note that the bead-magnet distances at which the calibration was extracted are in the same range as in the tissue mechanics measurements explained below. Although the scaling for the magnetic force, which closely follows $F(d) \propto r_b^3 d^{-4}$, seems in good agreement with the prediction for a magnetic point dipole interaction, this simple interpretation of the force curves is not applicable here for two reasons: first, the distances d investigated in the calibration curves of Figure S3 are comparable with the size of the magnet: $d \leq 2r_m$ and within this

¹Note that the terms $6\pi\eta_f r_b v(t)$ and $\frac{4}{3}\pi r_b^3(\rho_b - \rho_f)g$ balances each other in free fall, $v(t) = v_\infty$. We performed this falling ball viscometer experiment separately. We recovered from v_∞ the tabulated viscosity of glycerol to within 8%.

range, the magnet cannot be approximated by a point dipole; second, the magnetization of the steel ball is field dependent, hence a function of d . A detailed study of the bead-magnet interaction force will be included in a forthcoming article [4].

Measurement of mechanical properties of gut and mesentery tissue

The “methods” section of the main text summarizes the protocol used to prepare the tissue samples for uniaxial tensile tests. The steel beads were either handled with aspiration pipettes or with tweezers, depending on their size and were inserted into the gut tube using these handlers. To attach the beads to the mesentery, they were first apposed to a paper tissue imbibed with glue and quickly deposited onto the membrane, which was held at the meniscus surface of the Ringer buffer (while still immersed). Our methods to attach the steel bead on the sample ensures that the applied force is uniformly distributed across the sample section that is perpendicular to the direction of the force. In particular, this is true for the dissected strip of mesentery thanks to the thinness of the tissue. We thus avoid significant complications arising when other fixation techniques must be used [5]. The preparation of tissue samples for tensile test is delicate; a systematic approach to the manipulation of the sample and the beads will be the subject of a forthcoming publication [4].

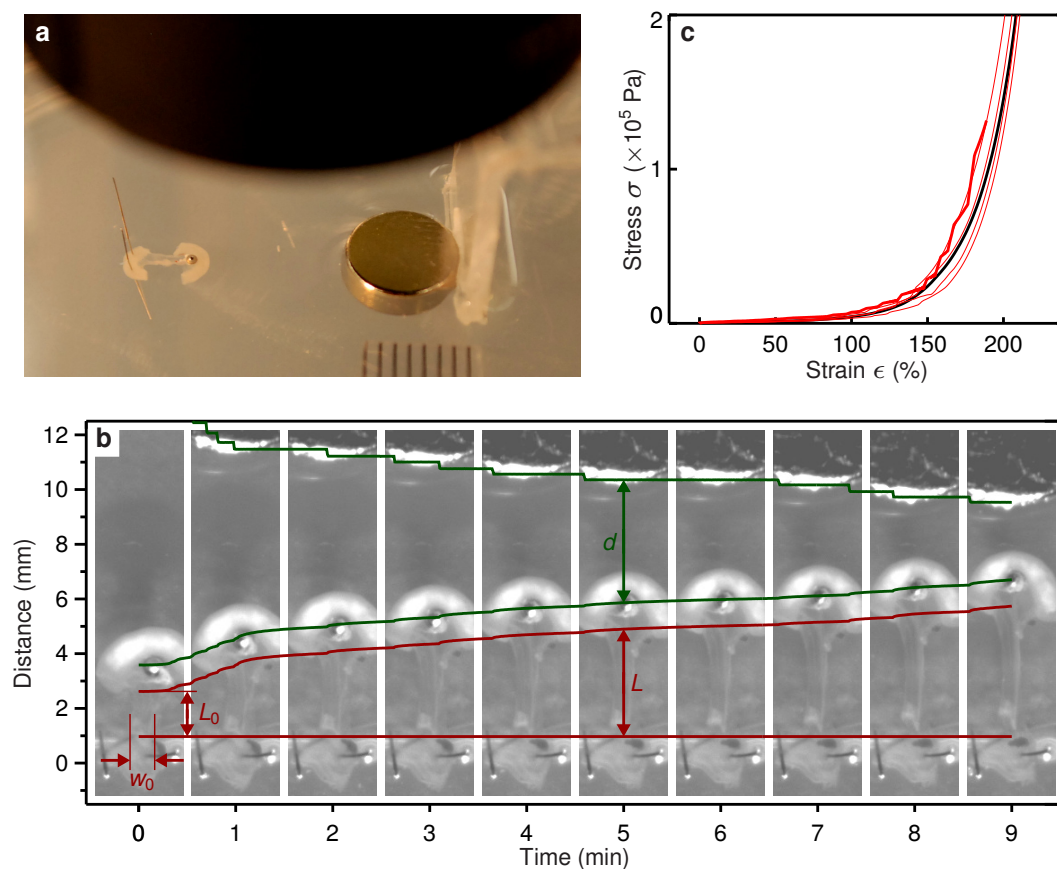


Figure S4 | Measurement of the mechanical properties of the mesentery, illustrated for chick E16. **a**, Ensemble view of the tensile test setup; the shadow is that of the microscope objective, along with the millimetric divisions of the ruler. **b**, The stepwise approach of the magnet stretches the sample by an amount L/L_0 that can be tracked as a function of the bead-magnet distance d . **c**, The resulting stress-strain mechanical response of the mesentery, as found for multiple samples (red), and the average (black) reported in Figure 3d of the main text.

Figures S4 and S5 show images from the procedure used for the measurement of the mechanical properties of the gut and mesentery tissue. The sample, to which the ball is attached, is laid out on the agarose gel and

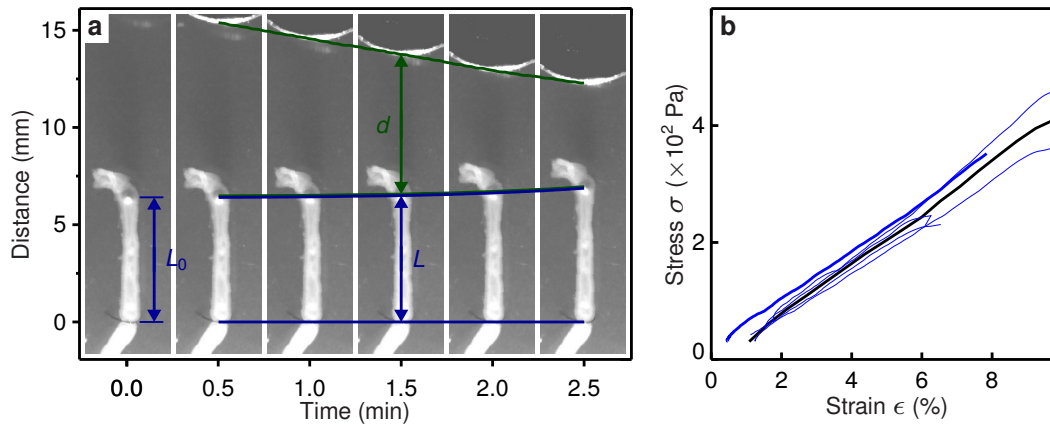


Figure S5 | Measurement of the mechanical properties of the gut tube, illustrated for chick E16. **a**, The approach of the magnet stretches the sample by an amount L/L_0 that can be tracked as a function of the bead-magnet distance d . **b**, The resulting stress-strain mechanical response of the tube, as found for multiple samples (blue), and the average (black) reported in Figure 3e of the main text.

immersed in the buffer (Figure S4a), while the magnet is brought towards the sample on the agarose gel along the strip's or tube's principal axis (Figs. S4b and S5a).

The supplementary movie 2 (S2.mov) shows a typical run for the tensile test on mesentery sample. Notably, the pre-conditioning stage, shown in the first 10 minutes of the movie time stamp, is commonly employed to produce reliable mechanical measurements relatively independent of previous manipulations [6, 7, 8]. Movies of the tensile tests were recorded using the digital camera at 2 frames per second (magnification of about $10\ \mu\text{m}$ per pixel) and the position of the magnet and the bead are tracked using the image registration method described in the previous section. This allowed us to monitor simultaneously the changes in sample length L and bead-magnet distance d , which correspond to a uniaxial tensile test of the material at low rate, $\frac{1}{L} \frac{dL}{dt} < 10^{-3}\ \text{s}^{-1}$, thus ensuring that we probe only static elasticity of the material (i.e. the Young's modulus) [6, 8].

Image analysis allows us to determine both the natural rest length of the sample L_0 and the width w_0 from the micrograph, (see Figure S4b and the supplementary movie 2 (S2.mov)). Using the calibration curve shown in Figure S3, we can deduce the force $F(d)$ applied to the sample as a function of the bead-magnet distance d . For the mesentery samples, we can evaluate the thickness at rest $h_0 = (1 + \epsilon_p)^{1/2} h$ from the measurement of the thickness h associated with physiological strain ϵ_p (Figure S2). Since the section area of the sample is known ($A_0 = w_0 h_0$ for mesentery strips, or $A_0 = \pi(r_o^2 - r_i^2)$ for the gut tube samples where the outer and inner radii r_o and r_i are extracted from micrographs (see Figure 3 of the main text)), we can determine the nominal stress $\sigma = \frac{F(d)}{A_0}$, and plot it against the nominal strain $\epsilon = \frac{L}{L_0} - 1$ to quantify the mechanical response of the material. More sophisticated methods to extract the local strain field could be used here, for example by tracking small features in the sample. However we infer that the nominal strain is sufficient to evaluate both the non-linear mechanical response of the mesentery material and its effective differential (linearized) elastic modulus associated with physiologically relevant deformations. This method produces reproducible results, with same-sample variations that are below sample-to-sample variations that we measured at about 50%. Several stress-strain response curves, corresponding to samples of mesentery extracted from different chick E16 embryos are shown in Figure 4c and conform the reproducibility of these results.

To assess the existence of inhomogeneity and anisotropy of the material properties in the mesentery, we measured the stretching stiffness at a location in various directions (thus probing tissue anisotropy), and at different locations in the mesentery (probing tissue heterogeneity) for a given embryonic stage. We could not detect a significant difference between samples extracted from the same embryo, but at different location in the gut. We find small differences between tangential and radial dissection (radial sample were generally stiffer) for samples extracted from the same embryo, although these small distinctions were in general less

than the sample-to-sample variations across different embryos. This slight anisotropy in the mesentery tissue is compatible with the radial orientation of the distinguishable fibers (or veins), that can be seen on the dissected mesentery shown in Figure 1c of the main text, but not qualitatively relevant for our study here (see Fig. S4).

The tube displays a visible radial non-uniformity in the tube cross sections shown in Figure 3b of the main text (clearly distinguishable on the E16 micrograph), and we thus questioned whether a possible non-uniformity of the tube's Young's modulus could bias our estimate of the bending stiffness. Some tube segments exhibit a residual curvature which was small, and we used such a curved sample from embryonic chick at day 16 to evaluate the bending stiffness directly from the force required to straighten the tube. If v_0 indicates the initial deflection of the tube from a straight line, and δ the relative displacement of the bead, then $F = \frac{E_t l_t}{v_0^2} \delta$ in the tube straightening regime of the tensile test². We indeed observe two regimes for the force-extension response of the curved tube. Prior to straightening, starting from a deflexion $v_0 \approx 1.5r_0$, we measure $\frac{dF}{d\delta} \approx 10^{-4}$ N, while the tube is straightened, and $\frac{dF}{d\epsilon} \approx 10^{-3}$ N once the tube is straight (note that $\delta \neq \epsilon$). The force-extension slope in the first regime yields a stiffness of $\frac{E_t l_t}{v_0^2}$ while the slope in the second regime yields a stiffness of order $\frac{4E_t l_t}{r_o^2 + r_i^2}$. Plugging the inner and outer tube radii values ($r_i = 230 \mu\text{m}$ and $r_o = 390 \mu\text{m}$, see Figure 3b of the main text) yields the same value ($E_t l_t = 5 \times 10^{-11} \text{ N} \cdot \text{m}^2$) for the bending stiffness in either case, thus validating our method of measuring the bending stiffness of the gut tube.

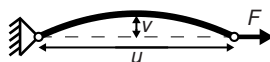
These measurements corroborate the conclusions, based on proliferation rates and presented in the main text, that the stretched mesentery applies a uniform compressive force along the rostro-caudal extent of the gut tube and does not induce individual loops via inhomogeneous differential tension. Furthermore, it allows us to model the mesentery and the gut as isotropic, homogeneous incompressible materials with a mechanical response that can be characterized solely in terms of their incremental Youngs moduli.

Computational model of gut looping

Since growth occurs over a period of days, inertial and viscous effects are negligible. When the gut is surgically separated from the mesentery, it relaxes to a naturally straight configuration while the mesentery shrinks to a slightly non-planar sheet; this is true at all stages of development prior to the formation of the fully developed loops. This implies that the looped configuration arises solely due to the fact that it is an energetic minimum (subject to the constraint of a vanishing linking number) of the composite system whose constituents grow relative to each other, and change their intrinsic morphometric and mechanical properties, over time. In other words, at each time points of development, the loop pattern results from the equilibrated arrangement taken by the composite membrane-tube system for the single values of their mechanical and geometric properties at this particular time point.

To build a computational model that predicts the loops pattern observed at a particular time point, given the mechanical and geometric properties of such composite system (at that time point) as input parameters, we follow a method described in detail elsewhere [9, 10]. That is, we approximate the elastic membrane by a discrete planar mesh of typically 300×60 equilateral-triangular elements. We approximate the tube by a similar planar mesh with different mechanical properties, made of exactly 2 rows of triangular elements (see Figure S6a where, following the conventions used throughout the paper, the tube is marked in blue and the membrane is marked in red). The elastic energy $F = F_m + F_t$ of the composite system is then the sum of the elastic energy of the membrane F_m and that of the tube F_t . In the following, we first summarize the algorithm used to obtain the configuration that minimizes energy. In particular, we justify our approximation of the tube by a 2-rows planar mesh. We then show the results of the simulations in two contexts: first an input

²Using the notations of the figure below,



we evaluate the bending moment by $8E_t l_t (v/u^2 - v_0/u_0^2)$, where (u_0, v_0) defines the configuration of the curved tube at rest with $v_0 \ll u_0$. The force applies a torque $2Fv$. Calling $\delta = u/u_0 - 1 \ll 1$ the initial relative displacement, and $L_0 \approx \sqrt{u^2 + (2v)^2}$ the invariant tube contour length, the moment balance reads $F \approx (E_t l_t / v_0^2) \delta$.

parameter sweep, that we used to get the data shown in figure 4 of the main text; and second, by using actual values of the input parameters, as measured on the chick gut at several time points, to visually compare the simulation with their real-life counterparts.

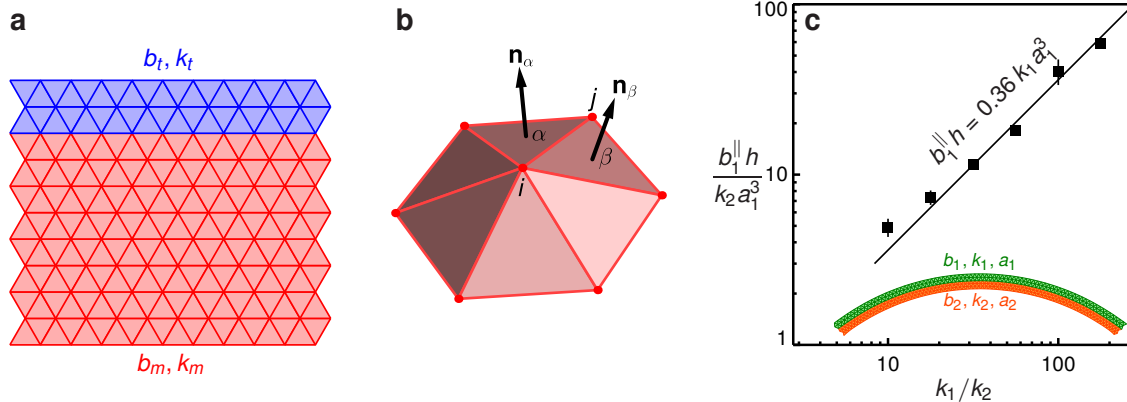


Figure S6 | Computational model for the gut-mesentery system and its calibration. **a.** The tube-membrane composite system is simulated by using a planar discrete triangular mesh, with an in-plane stretching stiffnesses k_t and an out-of-plane bending stiffness b_t for the tube (blue), and similarly stretching stiffness k_m and bending stiffness b_m for the membrane (red); see text for details and the relative magnitudes of these quantities. **b.** The discrete mesh approximation penalizes both in-plane and out-of-plane deformations; the extension/compression of springs ij connecting nodes i, j penalize in-plane stretching, while the relative orientation between the normals \mathbf{n}_α and \mathbf{n}_β of neighboring facets α, β penalize out-of-plane deformations. **c.** To calibrate the isotropic bending stiffness of the gut tube, and determine the relationship between k_1 and the in-plane bending stiffness b_1^{\parallel} we compare our simulations with a simple analytic relationship for the bending of a bimaterial strip (solid line, see text for details). Error bars, s.d.

The discretized “membrane” and its continuum limit

Following the notations defined in Figure S6b, we may write the elastic energy density of the membrane $F_m = F_{m,s} + F_{m,b}$ as the sum of the stretching energy density $F_{m,s} = \frac{\sqrt{3}k_m}{4} \sum_{ij} (r_{ij} - a_m)^2$, where r_{ij} is the distance between two nodes i and j and a_m is the natural rest length between nodes in the membrane (which can change as a consequence of growth), and the bending energy density $F_{m,b} = \frac{b_m}{\sqrt{3}} \sum_{\alpha\beta} (\mathbf{n}_\alpha - \mathbf{n}_\beta)^2$, where \mathbf{n}_α and \mathbf{n}_β are the unit normal vectors of the two facets α and β (see Figure S6b). The membrane material coefficients k_m and b_m are defined as $k_m = E_m h$ and $b_m = E_m \frac{h^3}{12}$ where E_m is the membrane Young’s modulus and h is the membrane thickness. In particular, b_m is the out-of-plane bending stiffness per unit width of the membrane. The parameters k_m and b_m can be obtained from the measurements of E_m and h on the real systems. The discrete representation of the membrane we use here has been shown in previous work to converge to the continuum limit of the so-called generalized Föppl-von Kármán equations used to describe the mechanics of thin plates that grow [9, 10], i.e. the discrete energy F_m converges to the elastic energy density of a plate in the continuum limit when $a_m \rightarrow 0$.

The discretized “tube” and its continuum limit

Similarly for the tube, $F_t = F_{t,s} + F_{t,b}$ with $F_{t,s} = \frac{\sqrt{3}k_t}{4} \sum_{ij} (r_{ij} - a_t)^2$ and $F_{t,b} = \frac{b_t}{\sqrt{3}} \sum_{\alpha\beta} (\mathbf{n}_\alpha - \mathbf{n}_\beta)^2$, where a_t is the natural rest length between nodes along the tube (and can change as a result of growth), and where the sums run over the elements belonging to the tube. The tube material coefficients $k_t = E_t \frac{\pi(r_o^2 - r_i^2)}{2r_o}$ and $b_t = E_t \frac{\pi(r_o^4 - r_i^4)}{8r_o}$, where E_t is the tube’s Young modulus and r_i, r_o are the inner and outer tube radii respectively. To assess the validity of the approximation we use here to represent the tube, we first need to ensure that the stretching

and the out-of-plane bending response of the simulated 2-row strip attached at the edge of the membrane, is mathematically equivalent to the continuum limit of an axially symmetric tube that can stretch, bend and twist, i.e. the in-plane and out-of-plane bending stiffnesses must be equal in our discrete representation of the tube (which is isotropic).

To calibrate and verify this we use the same discretization scheme as above, and perform a separate set of simulations of a different system: a bi-material composite strip, shown in Figure S6c. We attach a strip made of a 2-row planar triangular mesh of material 1, with mechanical stretching stiffness k_1 , out-of-plane bending stiffness b_1 , and spring rest length a_1 , to another strip made of a ν -row triangular mesh of material 2 with mechanical parameters k_2 (stretching), b_2 (out-of-plane bending) and a_2 (rest length). Both strips are assumed to have a thickness h . The width of the strip of the material 2 is chosen with $\nu < 10$, in contrast with the tube-membrane simulations described above where the membrane mesh is chosen as wide as possible. We introduce a mismatch strain $\epsilon_0 = \frac{a_1}{a_2} - 1$ and calculate the mechanically stable configurations of the bi-material composite by minimizing the total elastic energy using a damped molecular dynamics method [11]. For $b_1 \gg k_1 a_1^2$, $b_2 \gg k_2 a_2^2$, $\nu < 10$ and $\epsilon_0 < 100\%$, we observe that the bi-material composite beam bends in its plane with a uniform radius of curvature ρ (see inset of Figure S6c). In this regime we evaluate the effective in-plane bending stiffnesses per unit thickness, b_1^{\parallel} and b_2^{\parallel} of materials 1 and 2 respectively, from the measurement of ρ ; indeed a classical result due to Timoshenko [12] shows that the radius of the strip, $\rho = \frac{1}{\epsilon_0} \left[\frac{2a_1 + \nu a_2}{2} + 2h \frac{b_1^{\parallel} + b_2^{\parallel}}{2a_1 + \nu a_2} \left(\frac{1}{2k_1 a_1} + \frac{1}{k_2 \nu a_2} \right) \right]$. Additionally, we expect³ $b_1^{\parallel} \propto k_1$ and $b_2^{\parallel} \propto k_2$. Furthermore, in the regime $b_1^{\parallel} \gg b_2^{\parallel}$, corresponding to the case when the material 1 is much stiffer than the material 2, it follows $k_1 \gg k_2$, so that

$$\frac{\epsilon_0 \rho}{a_1} \approx \frac{2 + \nu}{2} + \frac{2}{\nu(2 + \nu)} \frac{b_1^{\parallel} h}{a_1^3 k_2} \quad (1)$$

and allows us to calculate b_1^{\parallel} from the radius ρ for various values of the parameters, as long as the aforementioned inequalities are satisfied⁴. The results of these simulations are shown in Figure S6c and fit the relation $b_1^{\parallel} h = 0.36 k_1 a_1^3$ for different values of $\epsilon_0 < 100\%$ and $3 \leq \nu \leq 9$ consistent with the continuum theory³; the slight difference from a perfectly linear relationship occurs at $k_1/k_2 \approx 10$ (see Figure S6c), where our approximation of Timoshenko's formula, equation (1), fails. Matching both the in-plane and out-of-plane bending stiffnesses of the 2-rows strip of material 1 (with width $2a_1$ and thickness h) yields $b_1^{\parallel} h = 2b_1 a_1$, so that $k_1 a_1^2 = 5.6 b_1$. This then is the relation between the parameters k_1 , b_1 and a_1 that characterize the 2-row edge strip as mathematically identical to an elastic tube of radius a_1 exhibiting an axially symmetric bending stiffness $2b_1 a_1$ attached along the edge.

Then k_t and b_t are related by the following relation: $k_t r_o^2 = \frac{4}{1 + (r_t/r_o)^2} b_t$. For both the biological and physical (i.e. rubber) experimental systems considered in our study, we measured that $0.3 < \frac{r_t}{r_o} < 0.6$, i.e. $2.9 b_t < k_t r_o^2 < 3.6 b_t$. These inequalities are in close agreement with the symmetry of the tube bending stiffness, that requires $k_t r_o^2 = 5.6 b_t$ as we just demonstrated with the bi-material strip, since the gut is typically very stiff in extension so that it can be modeled as being inextensible⁵. We further verified that changing the ratio $k_t r_o^2 / b_t$ by 40% did not actually significantly alter our results.

³In fact, one expects only small deviations, due to discretization errors, from the laws $b_1^{\parallel} h = k_1 \frac{(2a_1)^3}{12}$ and $b_2^{\parallel} h = k_2 \frac{(\nu a_2)^3}{12}$ (derived in continuum mechanics).

⁴If we take $a_1 = r_o$, $k_1 = k_t$, $b_1 = b_t$, $k_2 = k_m$, $b_2 = b_m$ and $\nu = \frac{\epsilon_0 \rho}{r_o} \gg 1$ for the width of membrane, as assumed in the main text, we obtain the scaling $\rho \sim \left(\frac{E_t h}{E_m h} \right)^{1/3} \epsilon_0^{\beta}$, with $\beta = -1$ as a consequence of the local torque balance [12]. The loop-wise force balance derived in the main text results in a similar scaling but with $\beta = -\frac{2}{3}$.

⁵For $k_t/k_m \ll 1$, the axial compression of the tube can reach a few percent thus effectively changing the mismatch strain between the membrane and the tube, while for both the biological gut and the rubber models, $k_t/k_m \gtrsim 1$ so that axial compression is negligible. In simulations performed with $b_t < 0.1$, and at input strains $\epsilon_0 < 10\%$, the loop radius is about 50% higher than the theoretical fit presented in Figure 4c of the main text, since the input strain is moderated by the tube axial compression. In this particular case we used the mismatch strain associated with the actual rather than the natural tube length, thus effectively excluding the effects of axial compression.

Building the membrane-tube composite

Growth of the tube and the membrane is simply modeled as a change in the rest lengths between the nodes, so that differential growth (and thus the induced mismatch strain) arises when there are spatial variations in these parameters in either the tube or mesentery, or because the rest lengths are not the same in the tube and the membrane. Since our experimental observations show that there are no spatial variations in either the growth of the edge of the mesentery or along the gut, but there is a mismatch strain ϵ_0 between the tube and the membrane, we set $\frac{a_t}{a_m} = 1 + \epsilon_0$. We then use a damped molecular dynamics method to minimize the system energy [11]. The resulting, mechanically stable, equilibrium geometrical configuration adopted by the composite system can then be recorded for the particular choice of input parameters k_m, b_m, k_t, b_t, a_t and ϵ_0 .

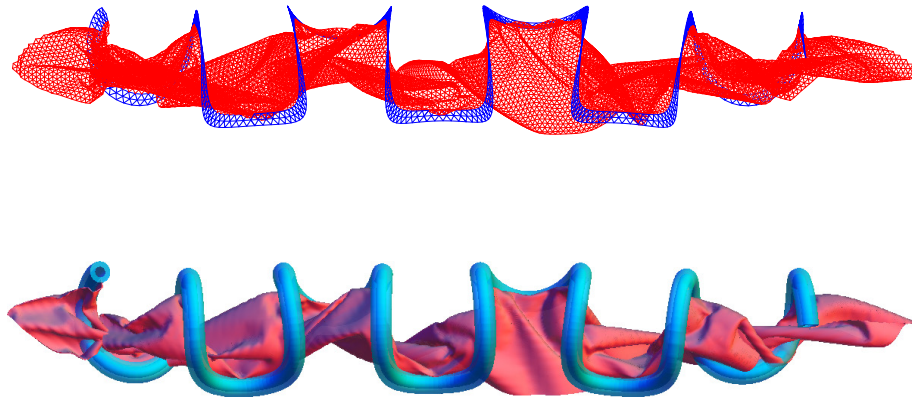


Figure S7 | Rendering of the mesh model. The top image represents a mesh calculated by our simulation procedure (this 3D image can be interactively manipulated in the PDF version; Adobe Reader 9.4 or higher is required), while the bottom image is the corresponding representation of the same configuration (from the same point of view), obtained using a rendering engine. The fine wrinkles in the mesentery are associated with its very small bending stiffness, but are energetically insignificant and do not effect the gut looping patterns.

Results: sweeping the parameter space

The simulations are first used to determine the equilibrated configurations of the tube-membrane system in a wide, yet realistic, range of input parameters values. For the membrane, in terms of the length scale $a_t = r_o$ and of the effective Young's Modulus $E_m \frac{h}{r_o}$, we find that the experimental bending stiffnesses of the membrane encountered in this study (for both the biological mesentery and latex sheet) in the range $10^{-5} < b_m < 10^{-3}$ has no detectable influence on the results presented here. Therefore we ran our simulations using the above set of units, where $k_m = 1$, with $b_m = 10^{-4}$ for the membrane, and $k_t = 5.6b_t$ for the tube where b_t varies between 2×10^{-2} and 10 to cover a wide range that encompasses the experimental values measured in our study. For each b_t chosen in this range⁵, we investigated values of ϵ_0 between 0 and 100%.

The supplementary movie 1 (S1.mov) present the resulting equilibrium geometries for various choices of these input parameters. Configurations with three values of b_t are represented⁶ at the top, center and bottom of each frame. The parameter ϵ_0 increases from one frame of the movie to the next while keeping the value

⁶When rescaled correctly, b_t is calculated as the ratio $\frac{E_t l_t}{2E_m h r_o^3}$ where $l_t = \frac{\pi}{4}(r_o^4 - r_i^4)$.

of b_t constant for each top, center and bottom configuration. We note that each frame presents equilibrium configurations of the composite system that have reached minimum energy for a particular set of parameters b_t, ϵ_0 . Thus the movie does not represent the approach to equilibrium, but is a series of actual equilibrated configurations adopted by the composite system, for the range of parameters shown in the accompanying graph. In this movie, and throughout the article, we use a blue tube to render the configuration adopted by the 2-rows strip along the edge of the mesh (consistent with our calibration of its isotropic bending stiffness as indicated above), and a continuous red membrane to render the remaining mesh of the composite system. Figure S7 shows a mesh configuration, direct output of the simulations, and its rendering following these conventions. We note that there are small boundary layers near the edges of the composite system where the loop radius and wavelength deviate from the values in the interior - these boundary layers arise since the edges are free. We also note that bending the mesentery out of the plane costs very little energy, and thus leads to the formation of many fine wrinkles [13], as observed in some of the rubber models. However, these are of no relevance in determining the gut looping pattern.

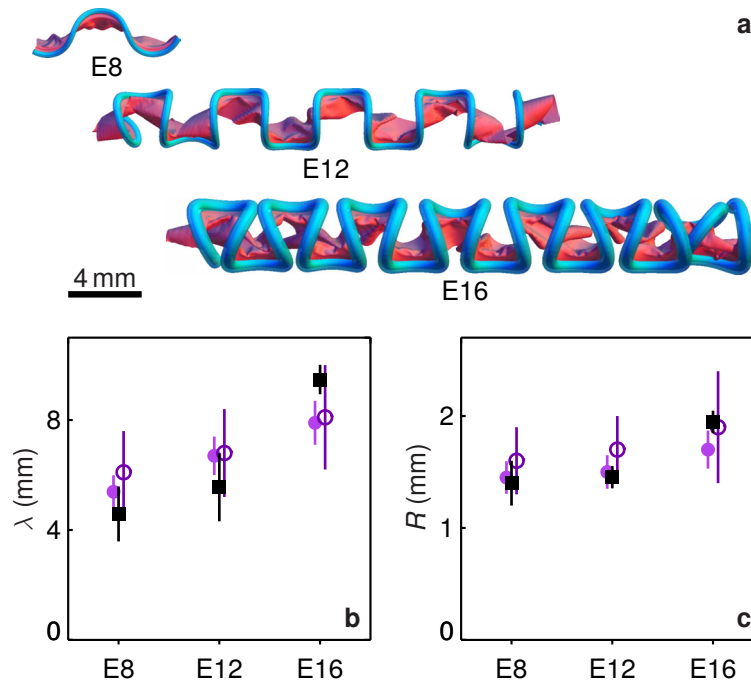


Figure S8 | Numerical evolution of the form of the chick gut. **a**, Equilibrated configurations of the tube-membrane system calculated numerically using the experimental measurements, performed on chick embryos at E8, E12 and E16, as input parameters. **b**, The loop contour wavelength λ measured from the embryos (squares), from the configurations shown in panel a (filled circles) and from the simple model (3) of the main text (open circles) at the three stages E8 – 12 – 16 of development (symbols are shifted horizontally to show the error bars; in the numerical model, error bars originate from the finite length of the simulated system that leads to small end corrections associated with the presence of boundary layers near the free edge, as expected). **c**, The loop radius R , symbols as in panel **b**. Error bars, s.d.

Results: simulating the chick guts at several time points of development

The mechanical parameters k_m, b_m, k_t, b_t are extracted from the morphometric and mechanical measurements performed at various time points during development (see main text and its Figure 3). In particular, we measure the mismatch strain as explained in the main text and Figure 3d using the fact that the mesentery has a periphery shorter than the tube extent when both lengths are measured upon their surgical separation (thus leading to a physiological mismatch strain ϵ_p , see main text). We then obtain ϵ_0 from linearizing the elastic response of the mesentery around the particular value of the physiological strain ϵ_p (see main text)⁷.

At different time points along the development of the gut, the mesentery thins, the tube thickens and simultaneously grows relative to the mesentery. Thus the mismatch strain ϵ_0 at a particular time point depends on the total differential growth between the gut and the mesentery. Similarly, the mechanical and geometrical parameters change as the gut develops. At every time point, mechanical equilibrium determines the gut morphology and our simulations can be used to determine the equilibrium shape of the gut-mesentery composite using the measured mechanical and geometrical parameters and the relative growth strain. Using the experimental values of the parameters $h, r_i, r_o, E_t, E_m, \epsilon_0$ at three time points *E8, E12* and *E16* of the chick gut development (see main text, where the data are summarized in Table 1), in Figure S8a we show the numerically obtained (equilibrated) corresponding configurations. This illustrates how we can track the evolution of gut development as a function of the measured mechanical and geometrical parameters that are input in our model. The simulated configurations closely match the shape of the real gut (see Figures 1a, 2c and 4a of the main text). In Figures S8b and c we show how the geometrical characterization of the loops evolves in terms of the contour wavelengths λ and radius R , at these three developmental time points, and the excellent parameter-free agreement with experimental measurements of these quantities in the chick gut. Ideally, we would of course like to predict the evolution of the geometry of the tube, the mesentery and the relative growth - but we have no theoretical basis for this at present.

Comparative mechanical properties of other species: quail, finch and mouse

For each quail, zebra finch, and mouse we selected two developmental time points representing an early and late phase of looping, where the latest stage chosen on the basis of the time after which the number of loop does not change anymore. For each animal, we repeated the morphometric and mechanical measurements, just as shown for the chick in the main text, and followed the gut development using the same methods for all species.

The results, shown in Figures S9 to S11 follow the same structure used in Figure 3 of the main text. We see that although the actual geometrical dimensions for the different animals are very different (see Figure 5 of the main text), there are similar trends in the morphometric characteristics across species: the thickness of the mesentery decreases with embryonic age, while the tube enlarges. The differential growth between the gut and the mesentery is characterized by the physiological mismatch strain between the tube and the perimeter of the mesentery $\epsilon_p = \frac{L_t}{L_m} - 1$ (L_t is the tube contour length, and L_m is the mesentery perimeter, see the main text) increases during embryonic development (ϵ_p increases with the embryonic age). The physiological strain falls between 100% and 200% at gut development maturation for all species studied here.

The mechanical properties of the tissues are of the same order of magnitude for the 3 birds, while the mouse tissue is in general softer. Although the detailed causes of this mechanical diversity are not investigated here, it is striking that the physiological stresses in the mesentery fall in the same range (~ 0.1 MPa) for all the species investigated in this study. This suggests that growth and properties of tissues might be regulated by mechanical feedback.

In the inset of Figures S9c to S11c, we report the volumetric growth of the gut and the mesentery. For the embryonic chick, we observe that the volume increase is well approximated by a simple exponential with growth rates of about 2.5% per hour for the tube, and about 1.5% per hour for the mesentery. The cell proliferation reported in Figure 1 of the main text indicates that at *E12*, about 200 cells in a volume $1 \text{ mm}^2 \times 10 \mu\text{m} = 10^4 \text{ pL}$

⁷Similarly, for the rubber simulacrum described in the previous section, the mechanical parameters are measured directly and the mismatch strain ϵ_0 is dialed in by stretching the membrane before it is stitched to the tube, which is kept unstretched, after which the composite system is allowed to relax to its equilibrium.

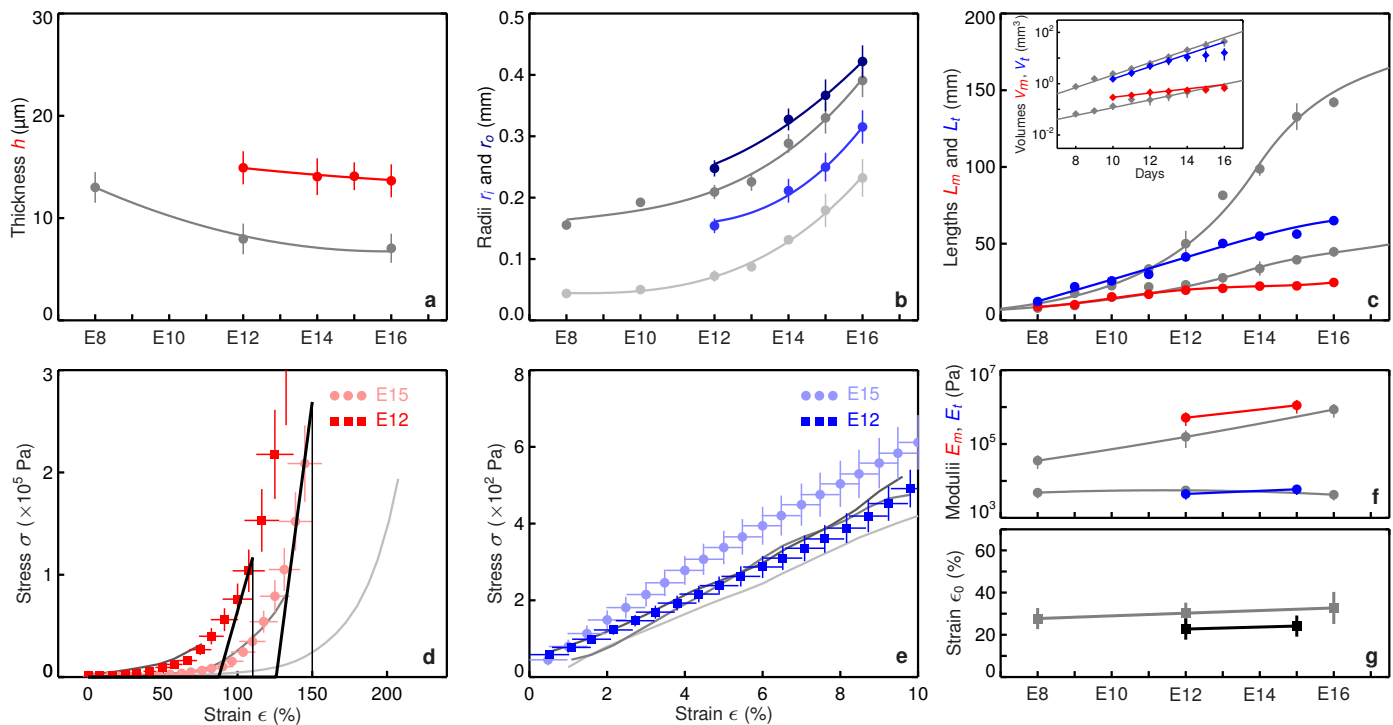


Figure S9 | Morphometric and mechanical measurements for quail at embryonic days E12 and E15. **a**, Mesentery thickness vs. embryonic day. **b**, Inner and outer tube radii vs. embryonic day. **c**, Tube and mesentery differential growth. **d**, Nominal stress vs. nominal strain response curves for the mesentery. **e**, Stress vs. strain response curves for the gut tube. **f**, Mesentery and tube effective Young's modulus vs. embryonic day. **g**, Effective differential growth strain vs. embryonic day. In all panels, the grey curves are the corresponding results for chick (E8, E12 and E16 are reported, see main text). Error bars, s.d.

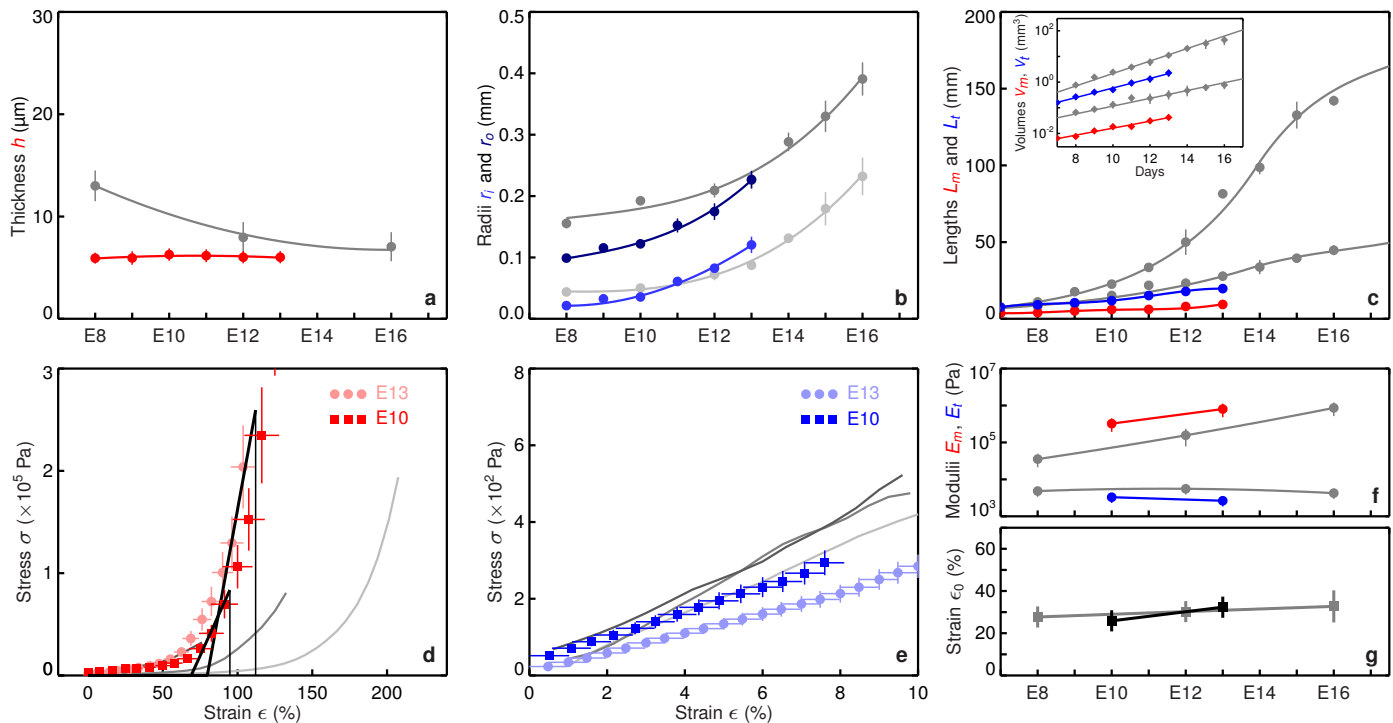


Figure S10 | Morphometric and mechanical measurements for finch at embryonic days E10 and E13. Panels are the same as in Figure S9.

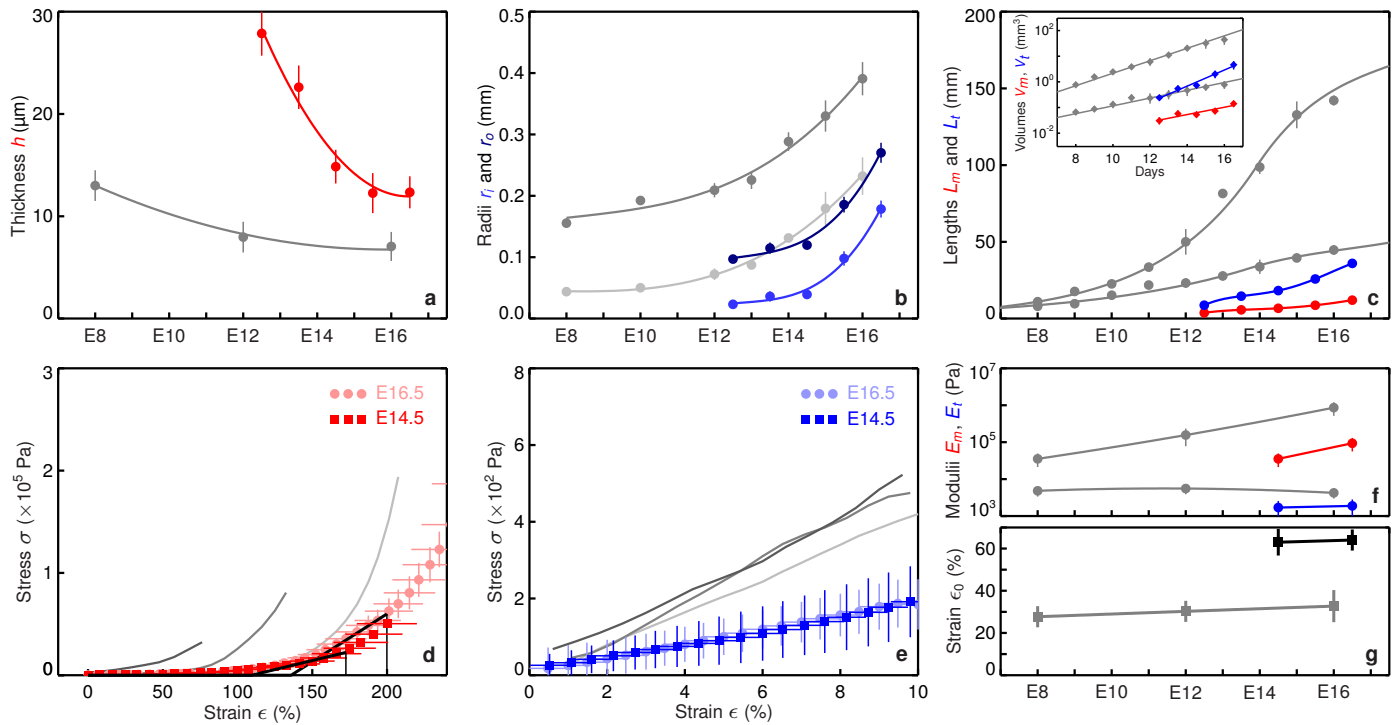


Figure S11 | Morphometric and mechanical measurements for mouse at embryonic days E14.5 and E16.5. Panels are the same as in Figure S9.

are created in the tube per unit generational (mitotic) time, while about 70 cells divide in the same volume of mesentery in the same time. Assuming mitosis takes ~ 1 h and an effective cell volume is ~ 1 pL, we thus obtain instantaneous volume growth rate of about 2% per hour in the tube and 1% per hour in the mesentery, in agreement with our direct volumetric growth rate measurement.

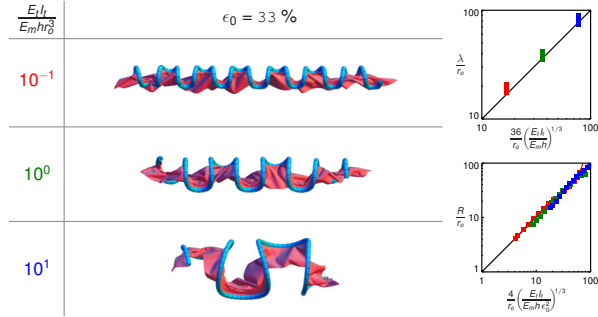
References

- [1] Crocker, J. C. & Grier, D. G. Methods of digital video microscopy for colloidal studies. *J. Colloid Interface Sci.* **179**, 298–310 (1996).
- [2] Xie, H. J., Hicks, N., Keller, G. R., Huang, H. T. & Kreinovich, V. An IDL/ENVI implementation of the FFT-based algorithm for automatic image registration. *Comput. Geosci.* **29**, 1045–1055 (2003).
- [3] Landau, L. D. & Lifshitz, E. M. *Fluid mechanics* (Pergamon Press, Oxford, England, 1987), 2nd edn.
- [4] Savin, T., Shyer, A. E. & Mahadevan, L. *In preparation*.
- [5] Lepetit, J., Favier, R., Grajales, A. & Skjervold, P. O. A simple cryogenic holder for tensile testing of soft biological tissues. *J. Biomech.* **37**, 557–562 (2004).
- [6] Fung, Y. C. Elasticity of soft tissues in simple elongation. *Am. J. Physiol.* **213**, 1532–1544 (1967).
- [7] Fung, Y. C. *Biomechanics : mechanical properties of living tissues* (Springer-Verlag, New York, 1993), 2nd edn.
- [8] Kenedi, R. M., Gibson, T., Evans, J. H. & Barbenel, J. C. Tissue mechanics. *Phys. Med. Biol.* **20**, 699–717 (1975).
- [9] Seung, H. S. & Nelson, D. R. Defects in flexible membranes with crystalline order. *Phys. Rev. A* **38**, 1005–1018 (1988).
- [10] Liang, H. & Mahadevan, L. The shape of a long leaf. *Proc. Natl. Acad. Sci. U.S.A.* **106**, 22049–22054 (2009).
- [11] Allen, M. P. & Tildesley, D. J. *Computer Simulation of Liquids* (Oxford University Press, New York, 1989).

- [12] Timoshenko, S. Analysis of bi-metal thermostats. *J. Opt. Soc. Am. Rev. Sci.* **11**, 233–255 (1925).
- [13] Cerda, E. & Mahadevan, L. Geometry and physics of wrinkling. *Phys. Rev. Lett.* **90**, 074302 (2003).

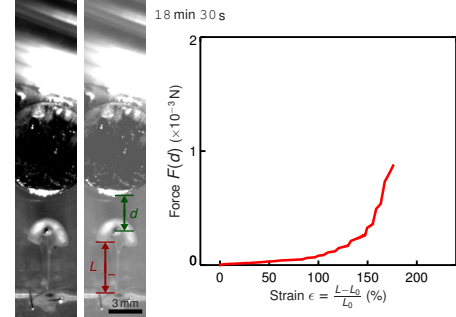
Supplementary Movies for “On the growth and form of the gut” by T. Savin et al.

(Click on the images to watch the movies)



Supplementary Movie 1 | Gut looping simulations.

Numerically computed equilibrium configurations of the gut-mesentery composite as a function of the differential growth strain between the gut and the mesentery for three representative values of the geometrical and mechanical parameters that characterize the system (see text, esp. Eq. (1)-(4) and SI for details). The top right sequence shows the length of the loops, while the bottom right sequence below shows the radius of the loops. We observe that the length of the loops does not change as a function of the differential strain (once past a threshold for the onset of the instability), but the radius decreases, as expected.



Supplementary Movie 2 | The measuring of the mechanical properties of tissues.

The movie on the left shows a sequence of displacements induced by a magnet on a bead that is glued to the tissue. Following calibration, this assay is used to measure the force-extension relation (shown on the right) for a piece of the mesentery, and thence its modulus.